



**An Overview of Target Chamber Design and
Analysis for the Light Ion Beam Laboratory
Microfusion Facility (Annual Report to Sandia
National Laboratories for Work Performed 10/1/88
- 9/31/89)**

**R.R. Peterson, R.L. Engelstad, J.W. Powers, H.Y. Khater,
M.E. Sawan, E.G. Lovell, G.A. Moses, J.S. Lipschultz**

February 1990

UWFDM-819

***FUSION TECHNOLOGY INSTITUTE
UNIVERSITY OF WISCONSIN
MADISON WISCONSIN***

DISCLAIMER

This report was prepared as an account of work sponsored by an agency of the United States Government. Neither the United States Government, nor any agency thereof, nor any of their employees, makes any warranty, express or implied, or assumes any legal liability or responsibility for the accuracy, completeness, or usefulness of any information, apparatus, product, or process disclosed, or represents that its use would not infringe privately owned rights. Reference herein to any specific commercial product, process, or service by trade name, trademark, manufacturer, or otherwise, does not necessarily constitute or imply its endorsement, recommendation, or favoring by the United States Government or any agency thereof. The views and opinions of authors expressed herein do not necessarily state or reflect those of the United States Government or any agency thereof.

**AN OVERVIEW OF TARGET CHAMBER DESIGN AND ANALYSIS FOR
THE LIGHT ION BEAM LABORATORY MICROFUSION FACILITY**

Annual Report to Sandia National Laboratories for Work Performed 10/1/88 - 9/31/89

Robert R. Peterson
Roxann L. Engelstad
John W. Powers
Hesham Y. Khater
Mohamed E. Sawan
Edward G. Lovell
Gregory A. Moses
Jeffrey S. Lipschultz

Fusion Technology Institute
University of Wisconsin - Madison
Madison, WI 53706-1687

February 1990

UWFDM - 819

1. INTRODUCTION

During the period between October 1, 1988 and September 30, 1989, the Fusion Technology Institute of the University of Wisconsin (UW) conducted research into issues related to a Light Ion Beam (LIB) driven Laboratory Microfusion Facility (LMF).^[1.1] This work consisted of two major components and some more minor efforts. The major components were:

- 1) Computational and experimental research into the damage to the first wall of the target chamber first surface due to the intense target generated x-rays,
and,
- 2) Computational study of the mechanical response of the target chamber structure to the microexplosion of the fusion target.

Other important parts of this work were calculation of neutron induced radioactivity in the target chamber structure and the resulting biological dose rates, and fragmentation of structures inside the target chamber due to the target x-rays. All of these are part of a long term effort to design a target chamber that can simultaneously meet the requirements imposed by LIB propagation and survive the effects of repeated microexplosions of fusion targets.

More detailed reports have been published elsewhere and may be consulted for more information on many of the topics outlined in this report. These reports are listed in Table 1.1. Some of these will appear in the proceedings of scientific meetings. At an appropriate point, some of this work will be published as refereed journal articles.

Table 1.1. Published Reports and Articles

1. R.R. Peterson, G.A. Moses and J.J. MacFarlane, "Blast Wave Simulations in Light Ion Laboratory Microfusion Facilities," *Bulletin of the American Physical Society*, Vol. 33, p. 2059, 1988.
2. R.R. Peterson, "Experiments to Simulate X-Ray Damage to the First Wall of the Inertial Confinement Fusion Laboratory Microfusion Facility," University of Wisconsin Fusion Technology Institute Report UWFDM-806, October 1989.
3. H.Y. Khater and M.E. Sawan, "Dose Rate Calculations for a Light Ion Beam Fusion

Laboratory Microfusion Facility," University of Wisconsin Fusion Technology Institute Report UWFD-809, October 1989.

4. R.R. Peterson, "Investigations into X-Ray Damage to the First Wall of the Inertial Confinement Fusion Laboratory Microfusion Facility," University of Wisconsin Fusion Technology Institute Report UWFD-816, October 1989.
5. R.R. Peterson, "X-Ray Effects on First Surfaces in the Inertial Confinement Fusion Laboratory Microfusion Facility," University of Wisconsin Fusion Technology Institute Report UWFD-818, December 1989.

The statement of work is listed below. The tasks have been completed to meet contractual obligations for this period. They are part of a multiyear project which has several other related tasks. The first item in the statement of work deals with design of plasma channels for propagation of ion beams in the APEX target chamber. Early in this period of research, work was terminated on the APEX project and experiments on plasma channels to be completed at SNL were never done. Therefore, by mutual agreement, no effort was devoted to Task 1. Instead, efforts were concentrated on target chamber issues for the LMF including topics not specified in the Statement of Work, such as calculation of radiological dose rates from neutron activation of the target chamber.

Statement of Work

1. Perform research on computer code work to aid development and understanding of APEX Z-pinch channel experiments. These channels are crucial in propagating high energy ion beams to an inertial confinement fusion target. These studies shall center on wall-confined Z-pinch channels with the option of a stabilizing, externally applied axial magnetic field. Nominal APEX channel parameter values (and their range of interest) are expected to be: channel current 100 kA (20 kA - 400 kA); channel radius 0.5 cm (0.35 cm - 3.0 cm); gas pressure 1 torr (0.3 - 30 torr); and the use of various gases. The parameters will be varied to optimize channel uniformity, channel stability without an ion beam, ion trapping capabilities, channel stability with an ion beam, minimization of ion beam energy losses and minimization

of ion beam quality degradation.

The Specific Technical Task is:

Develop as needed, maintain and run MHD codes to support the above Z-pinch channel work for the APEX project. Iterate parameter values as results are obtained for Z-pinch channel experiments at SNL.

2. Study the physics of rapid vaporization of LMF first wall material by target microexplosions.

Specifically:

A. Use the CONRAD computer code to consider the creation of vaporized wall material and the mechanical forces applied to the remaining wall surface by the process.

B. Work with scientists at SNL to devise experiments that will simulate the response of first wall materials. These experiments should simulate the rapid deposition of target x-rays, the resulting vaporization and the propagation of shock waves into the remaining wall material.

C. Use SNL computer codes to simulate the propagation of shocks into LMF first wall materials.

D. Consider how variations in target design will affect the survival of first wall materials.

R.R. Peterson will complete this task while visiting SNL.

3. Perform mechanical analysis of LMF chamber as a complete cylindrical shell using 2 1/4 Cr - 1 Mo steel and 6061-T6 aluminum. The following subtasks are to be included:

A. Calculate shell dynamic response from afterpressure including mean stresses. Assess validity of impulsive solution by comparison with numerical integration.

B. Revise cycle counting methods in existing fatigue code to accommodate mean stresses.

C. Perform fatigue stress analysis of chamber wall to determine an acceptable thickness for a lifetime of 3, 6, 9, 12 and 30 years.

4. Perform mechanical analysis of LMF chamber as a perforated cylindrical shell using 2 1/4 Cr - 1 Mo steel and 6061-T6 aluminum. Reconsider subtasks A, B and C of Task 3 using a modified Poisson's ratio and an effective elastic modulus to account for higher stresses in the

ligaments and increased flexibility.

5. Write a final report.

This report is in the form of an overview and is meant to tie different aspects of our work into an overall picture of the LMF target chamber design. Section 2 describes the overall target chamber design for the LIB LMF. Section 3 presents analysis of the target chamber gas response to the target explosion and predictions of the pressure loadings on the target chamber walls. In Section 4 the structural wall response to the pressure loadings and design of a wall for the SNL LMF target chamber are discussed. Section 5 deals with neutron activation of the target chamber and the resulting biological dose rates for various wall materials. In Section 6, results are presented for computational and experimental studies into effects of vaporization of wall material by the target x-rays. The fragmentation of structures in the target chamber by the target x-rays is discussed in Section 7 and conclusions are given in Section 8.

References for Section 1

- 1.1 B. Badger et al., "Target Chamber Studies for a Light Ion Fusion Laboratory Microfusion Facility," University of Wisconsin Fusion Technology Institute Report UWFD-768, August 1988.

2. LMF TARGET CHAMBER CONCEPT

The target chamber for the LIB LMF must be designed to simultaneously meet the ion beam propagation and target blast survival constraints.^[2.1] A picture of the current design is shown in Fig. 2.1. The general parameters are listed in Table 2.1.

The base case target chamber design is a 4.5 m high, 1.5 m radius circular cylindrical shell that is capped with 1.5 m radius hemispherical caps on both ends. The containment vessel is made of Aluminum 5083 or 6061-T6, which is 12.5 cm thick to withstand the pressure loading from the

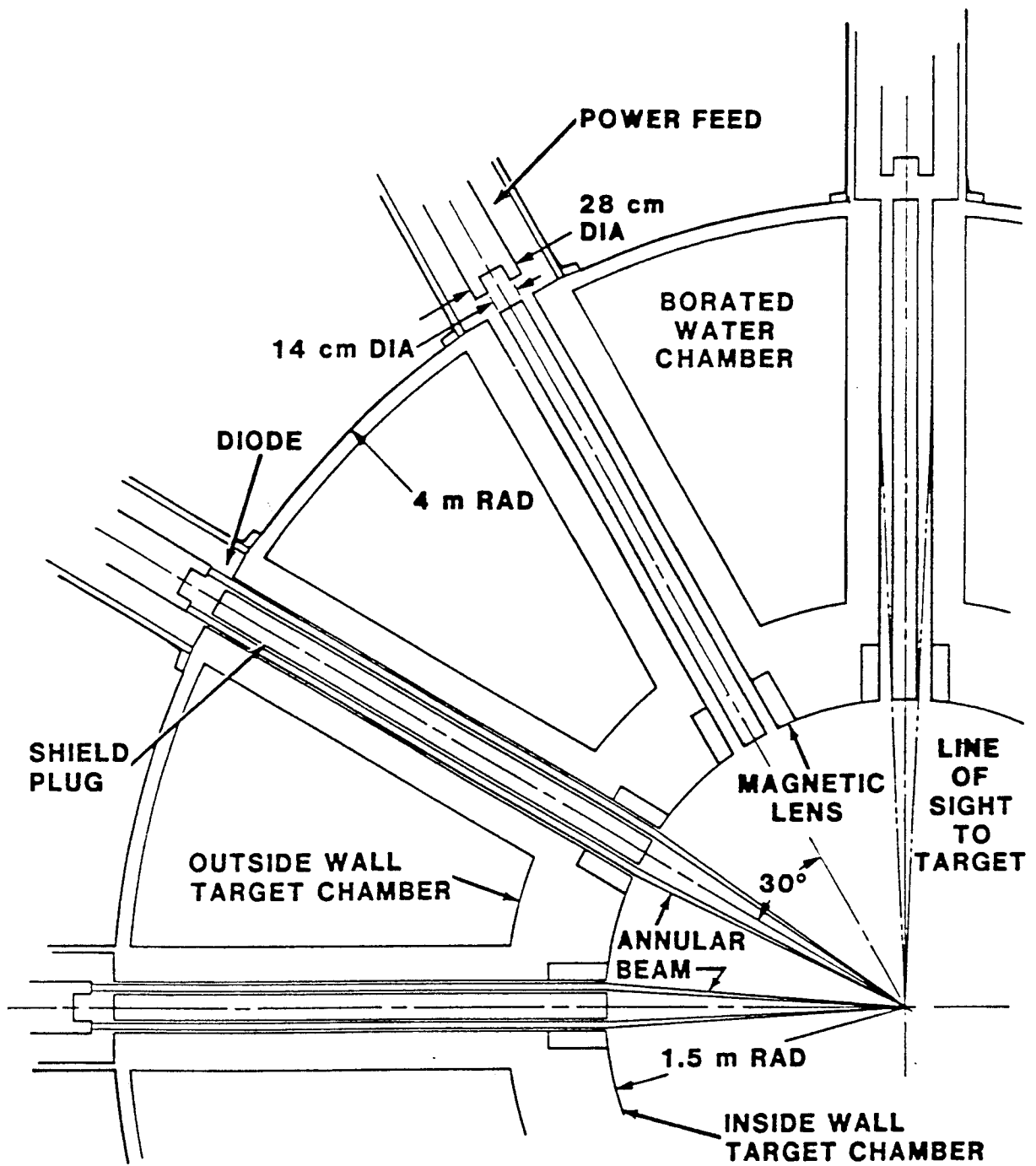


Fig. 2.1. Overhead view of the light ion fusion LMF target chamber.

Table 2.1. LMF Target Chamber Parameters

Geometry	Hemispherically Capped Cylinder
Radius	1.5 m
Height of Cylindrical Walls	4.5 m
Total Height	7.5 m
Wall Material	Aluminum 5083 or 6061-T6, 2 1/4 Cr - 1 Mo Steel
Wall Thickness	12.5 cm
Thermal Liner Material	4-D Woven Graphite
Thermal Liner Thickness	2 cm
Number of Beam Ports	36
Port Diameters	36 cm
Fill Gas	10 torr He

target explosion. This particular alloy has been chosen to minimize the radiological dose rate near the target chamber during the period a few days after operation of the LMF has ceased. The inner surface of the aluminum is lined with 2 cm of woven graphite. This graphite is to provide protection for the aluminum from vaporization by the target x-rays and from the damaging shocks that vaporization can generate. For the purposes of this study, the target chamber is assumed to be filled with 10 torr of helium gas, though there are indications that for proper beam propagation, the gas density should be reduced to 1 torr.

Propagation of the ion beam to the target is in a ballistic mode, where free electrons from the target chamber gas provide current and charge neutralization necessary for ballistic transport. The ballistic transport mode is currently favored over ion transport in plasma channels because of its relative simplicity and because it does not require additional structures inside the target chamber. The beam transport system carries the ion beams from ion diodes to the target. As seen in Fig. 2.1, the diodes are placed 4.0 m from the target and the ion beams come off the diodes in unfocused annular beams that are focused on the target by lens magnets.^[2.2] The lens magnets are placed 1.5

m from the target, which would focus a 6 mrad divergence beam over 1.5 m onto a 0.9 cm radius spot (roughly the size of the target). The 1-10 torr of helium target chamber gas provides the current and charge neutralization. The wall of the target chamber is placed in front of the lens magnets and, therefore, is at most 1.5 m from the target.

References for Section 2

- 2.1. B. Badger et al., "Target Chamber Studies for a Light Ion Fusion Laboratory Microfusion Facility," University of Wisconsin Fusion Technology Institute Report UWFDM-768, August 1988.
- 2.2 C.L. Olson, "Achromatic Magnetic Ions Systems for High Current Ion Beams," Proceedings of the 1988 Linear Accelerator Conference, Williamsburg, VA, October 3-7, 1988, to be published.

3. PRESSURE LOADING ON TARGET CHAMBER WALLS

The pressure loading on the target chamber first wall consists of at least two components that are in effect over different periods of time. Initially, the wall experiences a very high pressure pulse, perhaps in the megabar range, that has a width of only 10's of nanoseconds. This pulse is due to the creation and blow-off of a vapor layer by the intense x-ray pulse from the target. A second pressure pulse is due to the energy content of the vapor and target chamber gas in the target chamber pressure vessel. This pressure pulse will typically reach a peak of several bars and lasts 10's to 100's of milliseconds. The two components have impulses that are comparable.

The component of the pressure loading due to rapid x-ray vaporization is of concern because the pressures are so high that shock waves can be launched into the first surface material. These shocks could be damaging to the material. Therefore, the design includes a thermal liner of woven graphite that will protect the structural target chamber vessel from vaporization and will attenuate the shock before it reaches the vessel. The response of the thermal liner is discussed in Section 6. It is assumed that the shock strength is reduced enough that there is no shock launched into the vessel structure. It is also assumed that the pressure pulse which reaches the vessel wall is much

shorter than the typical period of vibration of the structure so that the pressure pulse can be treated as an impulse.

Preliminary calculations of the pressure impulse have been previously reported.^[3.1] The calculations were performed with the CONRAD computer code.^[3.2] In these calculations, the x-rays from the target are assumed to deposit instantaneously into the graphite liner. In these one-dimensional simulations, the wall was taken as a spherical surface 1.5 m in radius. The x-ray spectrum, which is what is expected to be radiated by a HIBALL type target, ^[3.3] is shown in Fig. 3.1. The target chamber gas is assumed to be 10 torr of helium, though there is very little absorption of the target x-rays by the chamber gas. These simulations used equation-of-state tables calculated by the IONMIX computer code.^[3.4] The unvaporized portion of the wall was treated as a immovable barrier. The peak pressure, the amount of mass vaporized, and the time-integrated impulse are shown plotted against total target yield in Fig. 3.2. The peak pressure from the vaporization for a target yield of 1000 MJ was 0.75 Mbar, which shows that the launching of shocks into the material is definitely possible. The impulse does not include the contribution from the residual pressure. The time dependence of the pressure is shown in Fig. 3.3, where it can be seen that the pressure pulse is less than 10 ns wide.

In addition to the very short pressure spikes due to vaporization, the target chamber gas imposes a lower peak but very long duration residual pressure on the first wall. The residual pressure, as will be shown in the following chapter, can have a very large effect on the mechanical response of the target chamber. Because it is an effect with a very long time scale and because the target chamber is not spherical, it is difficult to obtain the residual pressure from computer simulations with the CONRAD code. Instead it has been estimated that

$$P = (\gamma - 1) E/V \tag{3.1}$$

where P is the quasi-static residual pressure in the target chamber gas, γ is the ratio of specific heats for the gas, E is the thermal energy in the gas and V is the gas volume. E is the sum of the energy deposited in the gas by target x-rays and ions and the energy brought into the gas with

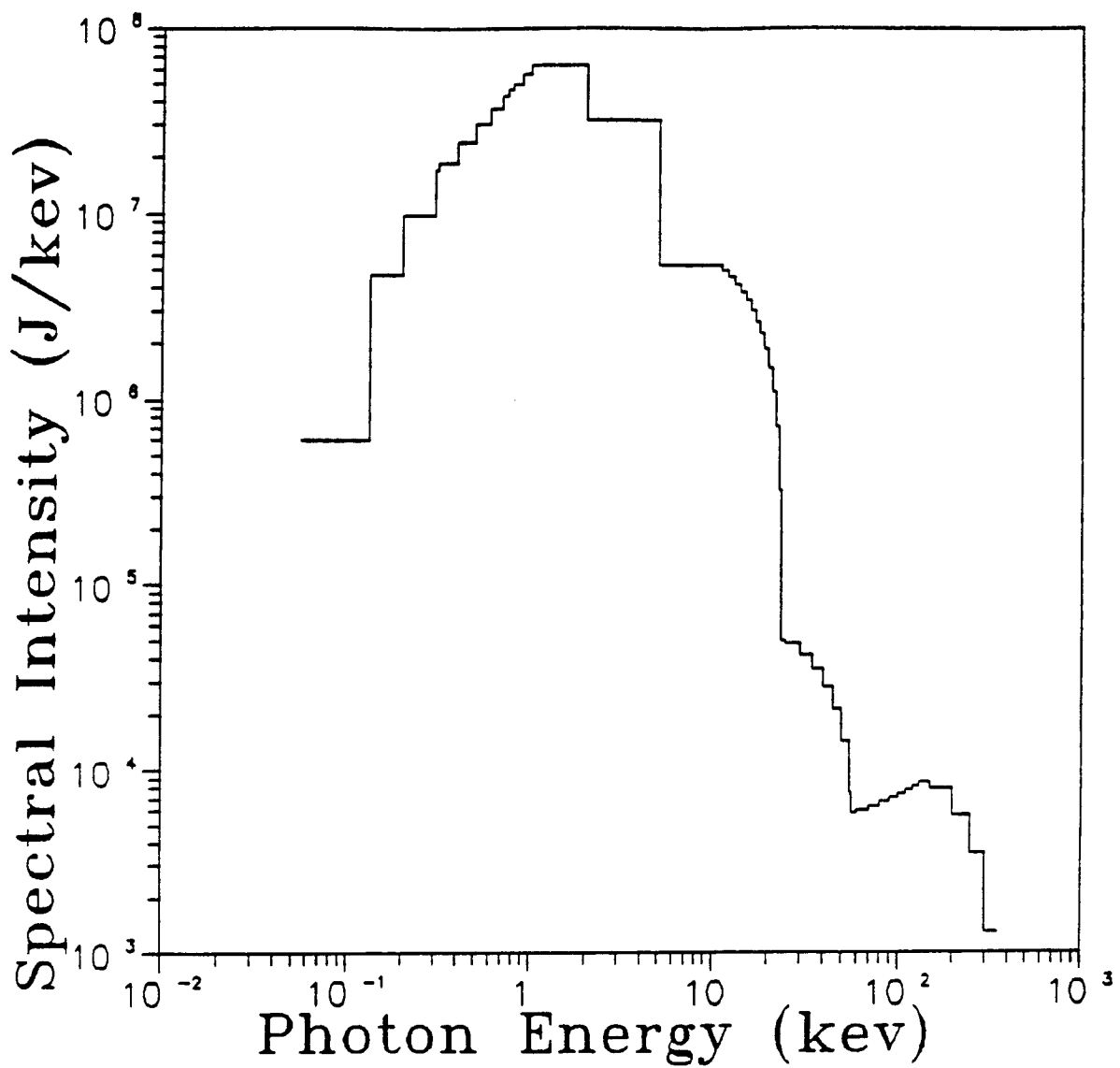


Fig. 3.1. Time integrated target x-ray spectrum from HIBALL type target.

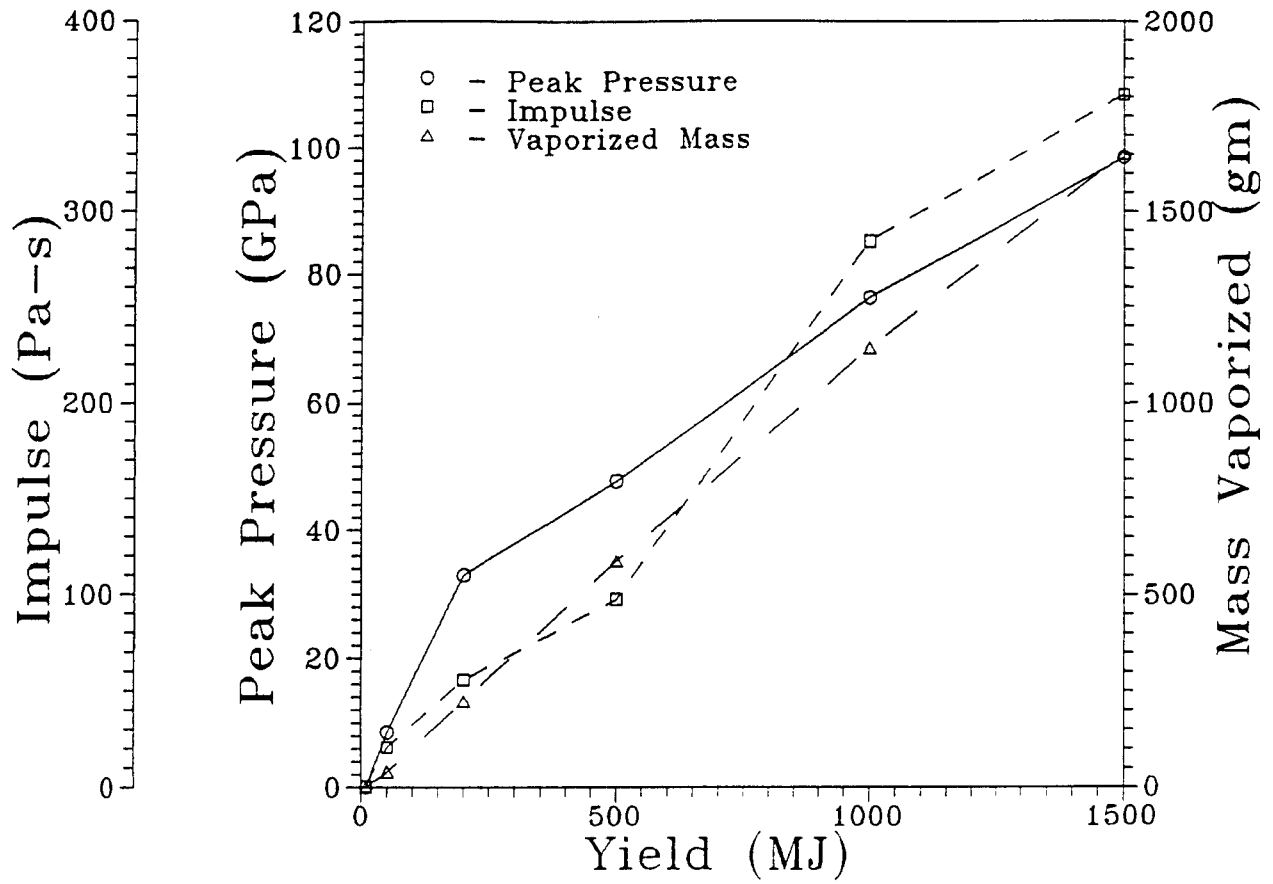


Fig. 3.2. Peak pressure, vaporized mass and impulse for a 1.5 m radius sphere versus target yield.

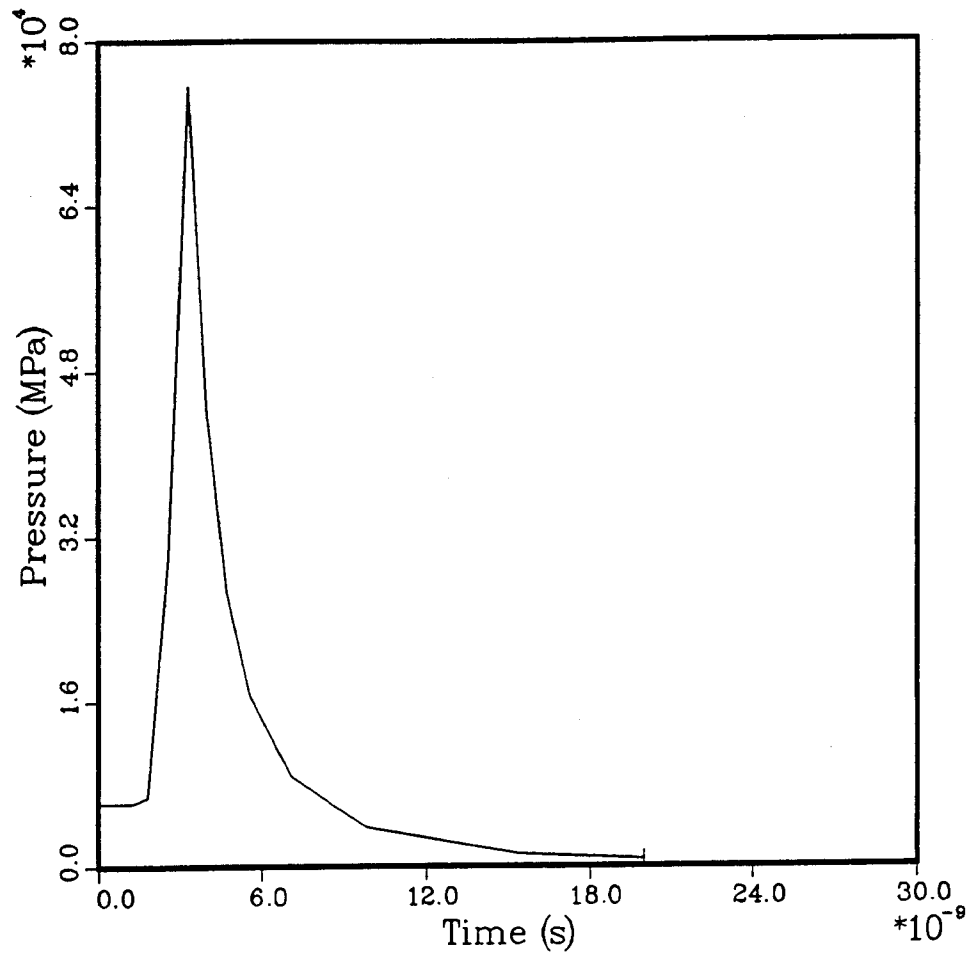


Fig. 3.3. Pressure at graphite wall versus time for 1000 MJ target yield and 1.5 m radius.

vaporized wall material, minus the energy radiated or conducted back to the wall. Here the result of a CONRAD simulation has been used for a spherical target chamber 1.5 m in radius to estimate E as 75 MJ, 150 μ s after the target explosion. The surface area of the actual target chamber is larger, possibly allowing more heat transfer out of the target chamber making this a conservative estimate. One should notice that there is considerable energy tied up in latent heat of vaporization of the wall material that is released when the vapor condenses. This energy is not part of E . For a cold monatomic gas or a fully ionized gas, γ is 1.67 and perhaps 1.2 for a partially ionized gas. The same CONRAD simulation would give a value of 1.47 and an average charge state of the gas of about 3. It cannot be definitively stated that this value for γ is either optimistic or conservative because when one takes the same 75 MJ and spreads it out over the larger volume of the actual target chamber, the gas will be colder but still partially ionized. Whether γ is higher or lower depends on the density of atomic states available to the new state of the gas. Because there is some uncertainty in γ , the residual pressure has been computed for γ equal to 1.2, 1.47 and 1.67. For V the volume used was for a 1.5 m radius cylinder, 4.5 m high and capped with 1.5 m radius hemispheres. Using the three values of γ , the estimates of the residual pressure are 0.326, 0.77 and 1.09 MPa. It is not believed that the gas will be cold enough to force the highest value of gamma, therefore, 0.77 MPa is taken to be the best estimate for the residual pressure. It is expected that the residual pressure on the wall will rise over a period of 10's to 100's of microseconds and to remain significant until most of the vapor has recondensed, which may take 100's of milliseconds. Because the history of the residual pressure is important to the structural response, this will be studied further with two-dimensional computer simulations that can account for the nonspherical target chamber. Also to be investigated is how changes in the target chamber geometry and gas venting schemes might change the nature of the residual pressure to the advantage of the target chamber design.

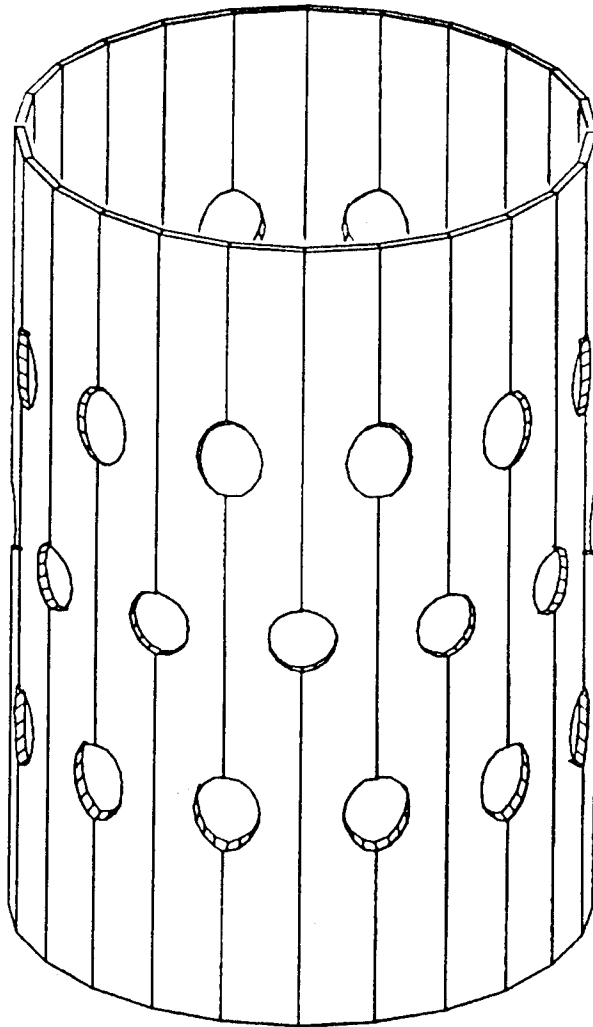
References for Section 3

- 3.1. B. Badger et al., "Target Chamber Studies for a Light Ion Fusion Laboratory Microfusion Facility," University of Wisconsin Fusion Technology Institute Report UWFD-768, August 1988.
- 3.2. R.R. Peterson, J.J. MacFarlane and G.A. Moses, "CONRAD - A Combined Hydrodynamics-Condensation/Vaporization Computer Code," University of Wisconsin Fusion Technology Institute Report UWFD-670, January 1986, Revised July 1988.
- 3.3. G.A. Moses, R.R. Peterson, M.E. Sawan and W.F. Vogelsang, "High Gain Target Spectra and Energy Partitioning for Ion Beam Fusion Reactor Design Studies," University of Wisconsin Fusion Technology Institute Report UWFD-396, November 1980.
- 3.4. J.J. MacFarlane, "IONMIX - A Code for Computing the Equation of State and Radiative Properties of LTE and Non-LTE Plasmas," University of Wisconsin Fusion Technology Institute Report UWFD-750, December 1987.

4. STRUCTURAL RESPONSE OF TARGET CHAMBER

As previously noted, the proposed LMF target chamber consists of a capped cylindrical shell that is 1.5 m in radius and 4.5 m in height. For the actual surface area of this chamber there are a relatively large number of beam ports of substantial size (Fig. 4.1). Thus, Task 4 of the Statement of Work was to assess the effect of these perforations on the dynamic response and fatigue lifetime of the chamber. In addition, the mechanical analysis was to include the effect of mean stresses produced by the long duration residual pressure loading on the cylinder wall (Task 3). A major effort was made to develop subroutines for the existing fatigue code to accommodate these features.

In Section 3, the two components of the pressure loading were described as being either a short duration impulse or a long duration afterpressure. Figure 3.3 shows a pressure load history for a 1000 MJ target yield. The duration of the initial "spike" of this pressure loading is on the order of a few nanoseconds. Thus, comparing this to the response time of the shell (or the natural



Radius: 1.5 m
Length: 4.5 m
No. of Beam Ports: 36
Beam Port Radius: 18.0 cm

Fig. 4.1. Proposed LMF chamber design.

period of vibration), the loading can be characterized by an impulse. Consequently, the dynamic response will be dependent upon the magnitude of the impulse but it will be insensitive to the shape of the pressure spike. In addition to this initial impulse, a steady afterpressure of a sizable amount follows. Since the exact rise time of this residual pressure is unknown, the loading function has been modeled as a dynamic step function, which is actually more severe. Table 4.1 shows the pressure loadings considered in this analysis for various target yields. The residual pressures, listed as P_{static} in the table, were computed by both the CONRAD code and Eq. 3.1. It is known that CONRAD will not accurately predict these residual pressures; therefore they are listed in Table 4.1 as "Overestimated." However, it is felt that the results of Eq. 3.1 give a better representation of the actual overpressures and are consequently given as the "Corrected" values in the table.

Table 4.1. Pressure Loadings on the LMF Chamber

Target Yield (MJ)	Impulsive Pressure (Pa-s)	Overestimated P_{static} (MPa)	Corrected P_{static} (MPa)
1000	284	2.5	0.77
200	55	0.7	0.22
50	10	0.2	0.062
10	0.7	0.02	0.0062

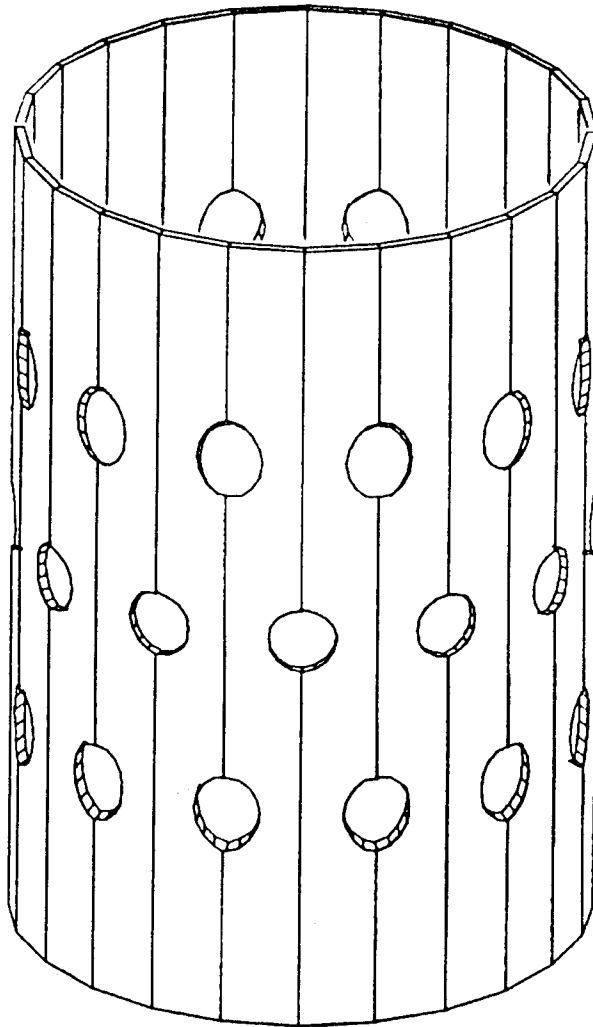
These pressure loads are assumed to be uniformly distributed over the first wall of the chamber, resulting in an axisymmetric mechanical response that is also symmetric with respect to the midspan plane. If the chamber is assumed to be rigidly supported at the ends, the largest stresses in the cylinder (due to bending) will occur near these supports. However, by increasing the wall thickness in these areas, localized stresses can be controlled. Thus, the basis for the design is the circumferential normal stress that is present at the midspan. It is also assumed that the longitudinal (or axial) stress will be zero at this location resulting in a uniaxial state of stress.

In order to account for the weakening effect of the shell perforations on the mechanical response of the chamber's first wall, modified effective elastic constants are used in place of actual material properties. These equivalent efficiency factors have been successfully used for years in the design of perforated tube-sheets and tube-plates.^[4.1-4.3] The method has been extended to the research here with the intent of determining an equivalent solid cylinder that can be analyzed by conventional shell equations. Two types of perforation patterns have been considered, i.e., triangular and square. These are shown in Fig. 4.2 with the pitch P defined as the distance between perforation centers and the ligament efficiency μ defined as

$$\mu = 1.0 - d/P \quad (4.1)$$

where d is the diameter of the perforation. With the numerical data for specific geometries being somewhat limited, ligament efficiencies of 0.33 and 0.40 have been used for the triangular and square perforation patterns, respectively. For the configuration and geometry of the LMF chamber, μ is actually 0.54. Thus the design is again on the conservative side. In fact with the lower ligament efficiencies used in the calculations, the design is comparable to a chamber with up to 15 beam ports (36 cm in diameter) in each of the 3 tiers, instead of the proposed 12 (see Fig. 4.1). Figures 4.3 and 4.4 show the data used for both the elastic modulus E^* and Poisson's ratio ν^* , as a function of the wall thickness, h .^[4.1] It is these curves, then, that are programmed into the fatigue code.

With the effective elastic constants known, the mechanical response of the shell can be computed. For example, Fig. 4.5 gives the circumferential stress history for an aluminum chamber with a square perforation pattern and a thickness of 13.0 cm. The loading in this case is only the short-duration impulsive pressure (284 Pa-s) corresponding to the 1000 MJ target. On the contrary, Fig. 4.6 shows the effect of a dynamic step load equivalent to P_{static} (0.77 MPa)



Radius: 1.5 m
Length: 4.5 m
No. of Beam Ports: 36
Beam Port Radius: 18.0 cm

Fig. 4.1. Proposed LMF chamber design.

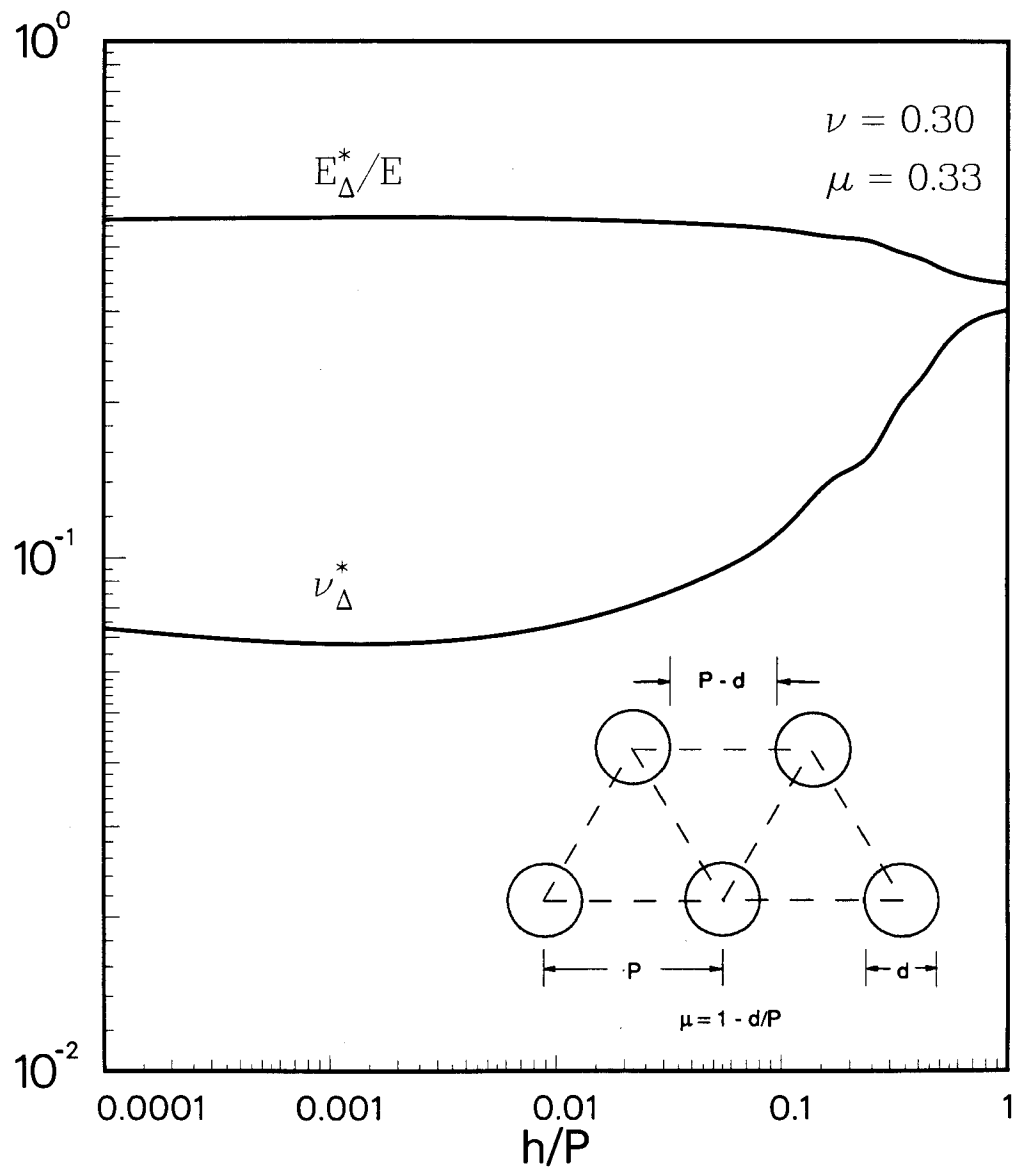


Fig. 4.3. Effective elastic constants for a triangular perforation pattern.

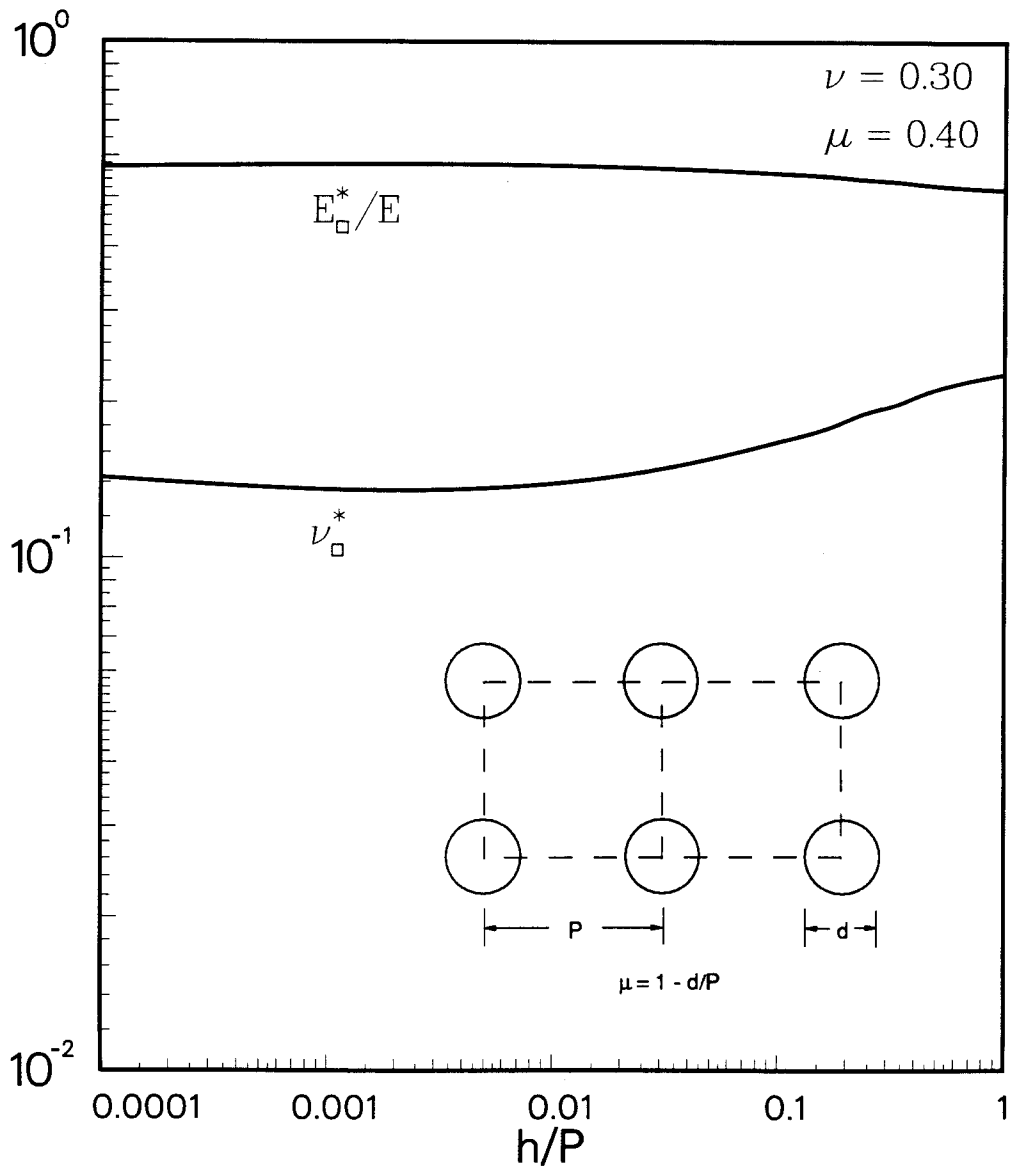


Fig. 4.4. Effective elastic constants for a square perforation pattern.

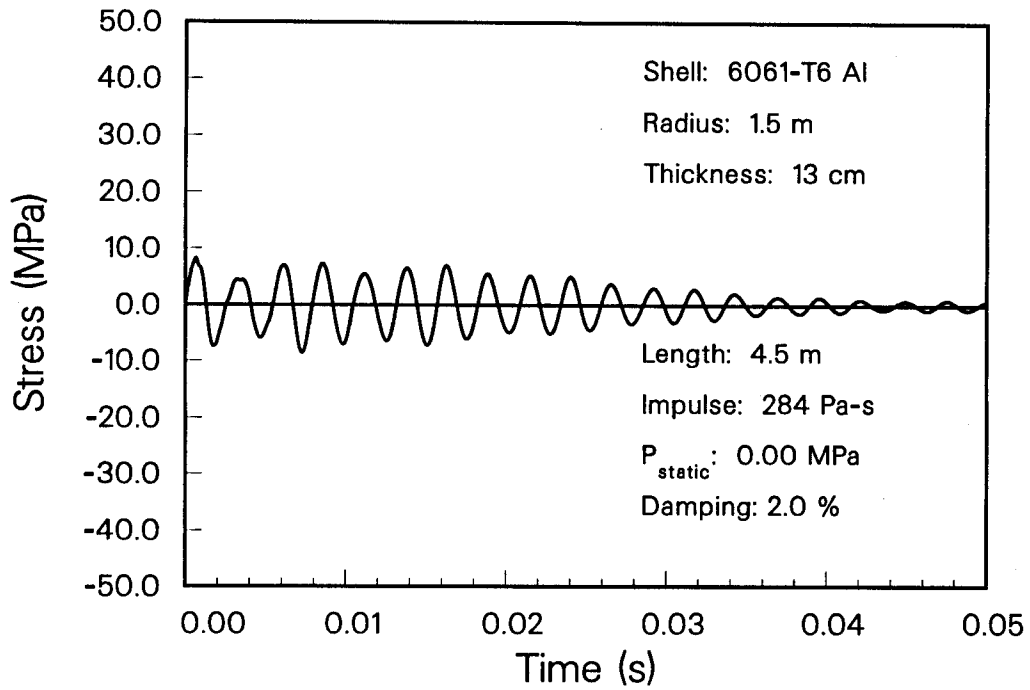


Fig. 4.5. Circumferential mechanical stress - the effect of impulsive loading only.

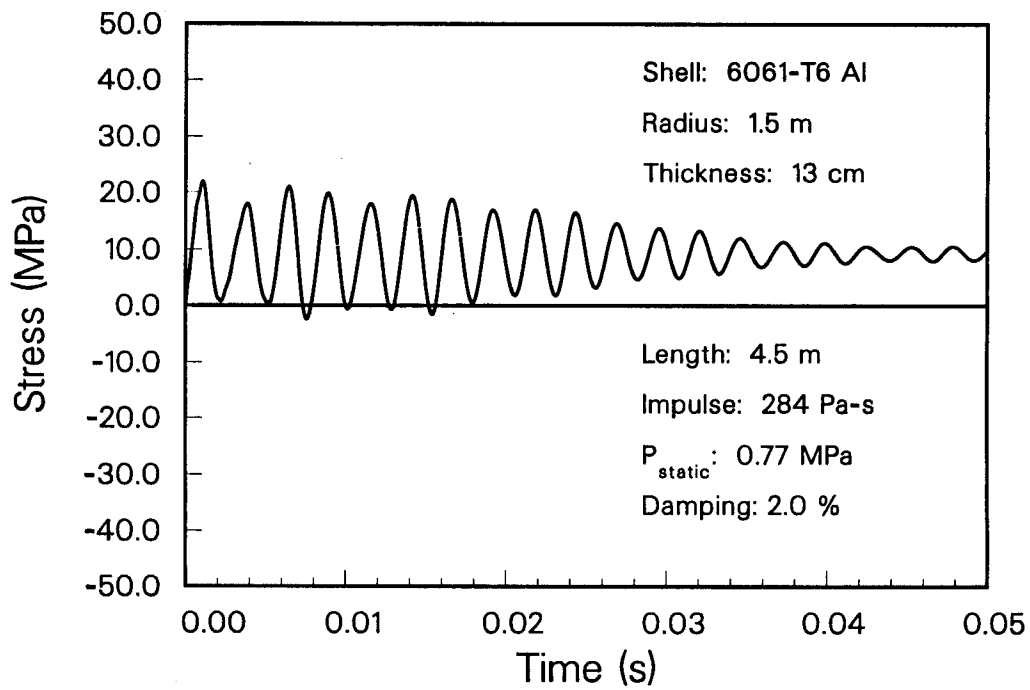


Fig. 4.6. Circumferential mechanical stress - the effect of impulsive loading and static pressure.

superimposed on the impulse load. Obviously, the initial transient stress has virtually doubled in magnitude, and the steady-state response is damping out to the equivalent value of the static stress due to the afterpressure. Consequently, what may seem like a relatively insignificant residual pressure, may actually produce a substantial mean stress in addition to amplifying the alternating stress. It is essential then to consider the mechanical stress history from both the short duration impulse loading and the long duration afterpressure in the fatigue calculations. Additionally, corresponding strain histories are determined by again employing the effective elastic constants.

Cumulative damage is used in the fatigue analysis since each stress/strain history is characterized by cycles of different amplitude and each target yield will produce a different history. Because of the mean stresses/strains present in addition to the alternating stresses/strains, an appropriate cycle counting method is used to determine an equivalent history that can be evaluated with the constant amplitude, fully reversed fatigue data. One of the most widely accepted methods, and one of the most accurate, is the rainflow method. The algorithm used to perform the rainflow cycle counting has been taken from the recommended procedures published by the American Society of Testing and Materials (ASTM).^[4.4] A Goodman diagram is used in conjunction with the cycle counting in order to obtain the value of the equivalent range stress/strain. Finally, Miner's rule is applied to estimate the linear, cumulative damage effects. This failure criterion can be expressed as

$$\sum_{j=1} (n/N_f)_j \leq D \quad (4.2)$$

where n is the number of applied cycles of loading conditions j , N_f is the number of design allowable cycles of the loading conditions and D is the allowable damage limit. Thus, failure is predicted if the total damage is greater or equal to 1.0.

It should be noted that the procedure outlined above (for the fatigue lifetime calculations) is consistent with the intent and methodology of the ASME Pressure Vessel Code.^[4.5-4.6] Safety

factors of either two on stress/strain or twenty on cycles is specified by the code; however, for the type of loading conditions on the LMF chamber, a factor of safety of two is more conservative. Further details of the fatigue analysis, including the rainflow method and the Goodman diagram, can be found in Ref. 4.7.

Two materials were considered in the structural analysis of the LMF chamber, 2 1/4 Cr-1 Mo steel and 6061-T6 aluminum. Figure 4.7 shows the strain-based fatigue data for 2 1/4 Cr-1 Mo that was published by Booker et al., at ORNL.[4.8] The data was obtained from completely reversed loadings with constant amplitude strains applied at the rate of $4 \times 10^{-1}/s$. The latest fatigue data on welded Al 6061-T6 was obtained from the Aluminum Association and is shown in Fig. 4.8.[4.9-4.10] The data (stress-based) was given for "Category B" type welded joints, which are defined as:

"Base metal and weld metal at full-penetration groove welded splices as transitions in width or thickness, with welds ground to provide slopes no steeper than 1 to 2 1/2, with grinding in the direction of applied stress, and with weld soundness established by nondestructive inspection." [4.9]

The lower 95% confidence limit, as shown on the curve, has been used in all fatigue calculations. In addition, the Aluminum Association recommends that the maximum range stress should not exceed 12.0 ksi (82.8 MPa).

Fatigue calculations were carried out for lifetimes of 3, 6, 9, 12 and 30 years. Table 4.2 shows the cumulative shots for each of the target yields considered. The pressure loading on the chamber for each yield consists of the "Impulsive Pressure" and the "Corrected P_{static} " from Table 4.1. In addition, both the triangular and the square perforation patterns were evaluated. Table 4.3 gives the minimum wall thickness needed for the steel, with the corresponding results for aluminum given in Table 4.4.

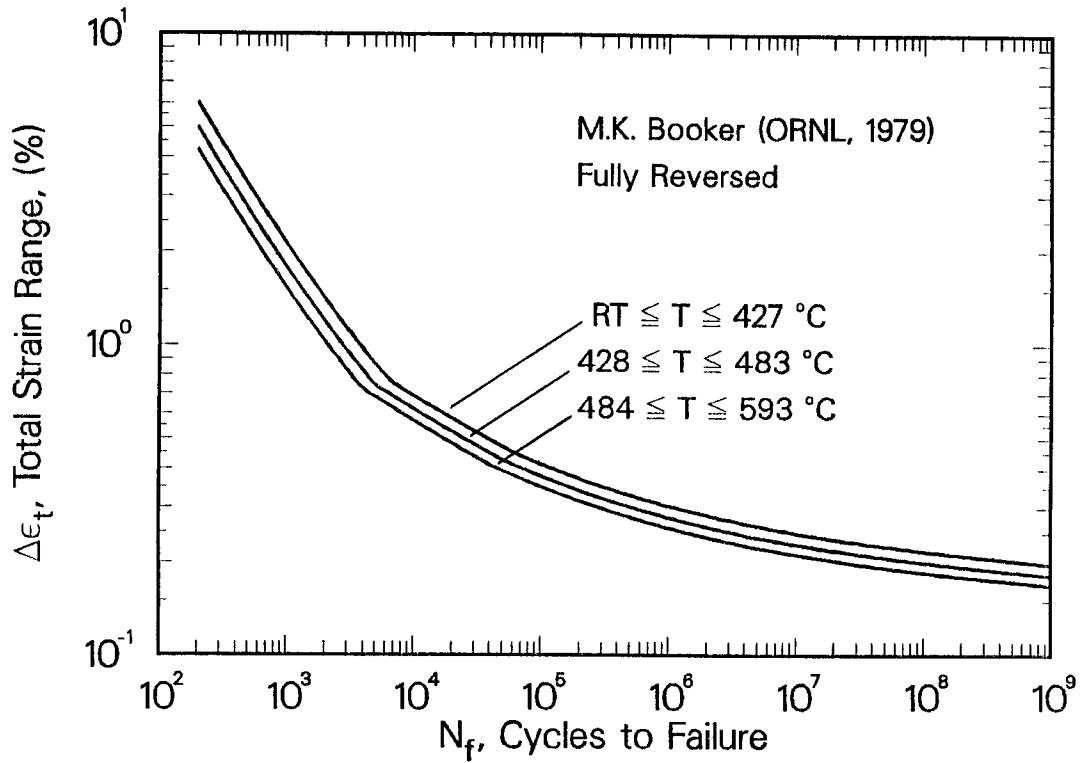


Fig. 4.7. Fatigue data for 2 1/4 Cr - 1 Mo steel.

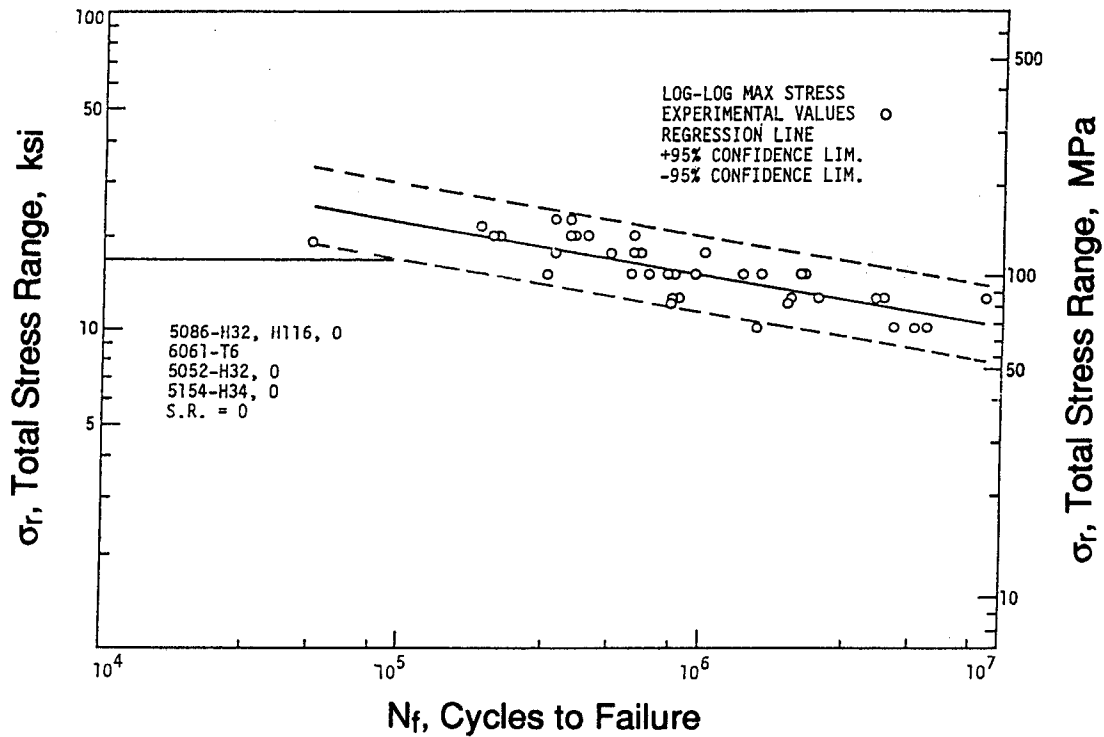


Fig. 4.8. Fatigue data for welded 6061-T6 aluminum.

Table 4.2. LMF Cumulative Shots

Lifetime Years	Target Yield			
	10 MJ	50 MJ	200 MJ	1000 MJ
3	990	480	30	0
6	1800	1080	90	30
9	1950	2130	330	90
12	2010	2970	810	210

Table 4.3. LMF Chamber Lifetimes for 2 1/4 Cr - 1 Mo Steel

Triangular Perforation Patterns	
<u>Lifetime Years</u>	<u>Minimum Wall Thickness</u>
3	0.6 cm*
6,9,12,30	2.4 cm*
Square Perforation Patterns	
<u>Lifetime Years</u>	<u>Minimum Wall Thickness</u>
3	0.5 cm*
6,9,12,30	1.8 cm*

*Thickness of 3 cm is recommended.

Table 4.4. LMF Chamber Lifetimes for Al 6061-T6

Triangular Perforation Patterns	
<u>Lifetime Years</u>	<u>Minimum Wall Thickness</u>
3	4.0 cm
6,9,12,30	21.0 cm

Square Perforation Patterns	
<u>Lifetime Years</u>	<u>Minimum Wall Thickness</u>
3	3.0 cm
6,9,12,30	12.5 cm

The results of the fatigue calculations were governed by the loadings of the 1000 MJ shots for both the steel and the aluminum, the primary failure mode being yielding. This is why the value of the thickness remains the same for lifetimes of 6, 9, 12 and 30. However, with no 1000 MJ shots present in the first 3 years, the value of the minimum thickness drops significantly. It should also be noted that the results of the fatigue calculations with steel show that the chamber can be built with a thickness of 2.4 cm or less. This is not recommended at this time; a thorough buckling analysis has not been completed. Therefore, it is assumed that the thickness of the chamber should be at least 3 cm.

In addition to considering a more detailed buckling investigation, a number of refinements can still be made to the fatigue code. One refinement would be an algorithm to more accurately assess the natural frequencies of the shell, to include the perforations and additional support structure. Ligament stresses and biaxial stress effects can also be better characterized by using finite element methods. Finally, further design options should be investigated to both reduce the afterpressure (e.g., larger volume chamber or venting schemes) and strengthen the shell in the perforated regions.

References for Section 4

- 4.1. F. Osweiler, "Evolution and Synthesis of the Elastic Constants, Concept from 1948 to Present - New Design Curves for Triangular and Square Patterns," *Design and Analysis of Piping, Pressure Vessels, and Components*, Proceedings of the 1987 Pressure Vessels and Piping Conference, Vol. 120, pp. 137-144, 1987.
- 4.2. P. Meijers, "Refined Theory for Bending and Torsion of Perforated Plates," *Pressure Vessel Components Design and Analysis*, Proceedings of the 1985 Pressure Vessels and Piping Conference, Vol. 98-2, pp. 11-19, 1985.
- 4.3. W.J. O'Donnell, "Perforated Plates and Shells," *Pressure Vessels and Piping: Design and Analysis a Decade of Progress*, ASME, New York, NY, Chapter 4, pp. 1041-1101, 1972.
- 4.4. "Standard Practices for Cycle Counting in Fatigue Analysis," *1988 Annual Book of ASTM Standards*, American Society for Testing Materials, Vol. 3.01, Designation: E 1049-85, pp. 764-772, 1988.
- 4.5. ASME Boiler and Pressure Vessel Code, Section III, Nuclear Power Plant Components.
- 4.6. ASME Boiler and Pressure Vessel Code, Case Interpretations, Code Case N-47, 1974.
- 4.7. J.W. Powers, R.L. Engelstad and E.G. Lovell, "Structural Design Considerations for the Sandia Laboratory Microfusion Facility's Target Chamber," University of Wisconsin Fusion Technology Institute Report UWFD-820, in press.
- 4.8. M.K. Booker, J.P. Strizak, C.R. Brinkman, "Analysis of the Continuous Cycling Fatigue Behavior of 2.25 Cr-1 Mo Steel," Oak Ridge National Laboratory Report ORNL-5593, Oak Ridge, TN, 1979.
- 4.9. W.W. Sanders, Jr. and J.W. Fisher, "Development of Recommended Specifications for Fatigue Design of Aluminum Structures," submitted to the Aluminum Association, October 1985.
- 4.10. "Specifications for Aluminum Structures," Aluminum Construction Manual, Fifth Edition, The Aluminum Association, 1986.

5. NEUTRON ACTIVATION AND DOSE RATES

The LMF is designed to contain target fusion reaction yields between 10 and 1000 MJ. This corresponds to the production of up to 3.6×10^{20} (14.1 MeV) D-T neutrons per shot. Based on 500 shots per year, the facility is expected to accumulate approximately 15,000 shots over a thirty year time period. The level of induced radioactivity produced from the interaction between the high energy neutrons and surrounding materials is of a great concern to the facility designers. The level of contact dose in the vicinity of the target chamber plays an important role in the process of selecting the target chamber wall material.

Here one ferritic steel alloy (2 1/4 Cr-1 Mo), and two aluminum alloys (Al 6061-T6 and low activation Al 5083) were considered as candidate materials for the target chamber wall. The chamber wall thickness differed with the different materials used. Chamber walls made of ferritic steel or aluminum were assumed to have thicknesses of 3 or 6 cm, respectively. The inner surface of the chamber wall is protected by a 2 cm thick graphite liner. In all cases a 1 cm thick sheet of boral (a B₄C-Al mixture) is placed on the outer surface of the wall. The target chamber is submerged in a borated water pool for neutron shielding. The borated water contains boric acid (H₃BO₃) at a concentration of 5 g/100 cm³. The boron in both the borated water and boral is enriched to 90% ¹⁰B for enhanced thermal neutron absorption.

Neutron transport calculations have been performed for the LMF chamber using the one-dimensional discrete ordinates neutron transport code ONEDANT^[5.1] together with the Los Alamos National Laboratory (LANL) MATXS5^[5.2] cross section data library processed from the ENDF/B-V evaluated files. The standard LANL 30 neutron- 12 gamma group structure was used and the calculations were performed using the P₃ - S₈ approximation. The problem has been modeled in spherical geometry with a point source at the center of the 1.5 m radius chamber. The energy spectrum of the neutrons emitted from the HIBALL target ^[5.3] was used to represent the source for the chamber calculations. The results were normalized to the average target yield of 200 MJ which corresponds to 7.1×10^{19} D-T fusions per shot. It should be pointed out that since shots of different yields are to be used in LMF, knowledge of the operational schedule before shutdown is essential for proper estimation of the dose after shutdown. The worst case conditions can be assessed by renormalizing the results to 1000 MJ assuming that the high yield shots will take

place right before shutdown.

The neutron flux obtained from the neutron transport calculations has been used in the activation calculations. The calculations were carried out by using the DKR-ICF^[5.4] computer code with activation cross sections taken from the ACTL^[5.5] library. The neutron transmutation data is given in 46 group structure format. The decay and gamma source data is taken from the table of isotopes with the gamma source data being in 21 group structure format. The radial build used in both of the neutronics and activation calculations is shown in Fig. 5.1. The calculations have been performed for one year of operation with 500 shots. The pulsing schedule considered here allows for two shots per day which are 6 hours apart with 18 hours between the daily shots. Operating for 5 days a week results in ten shots per week. Therefore, fifty weekly pulse sequences, which are 66 hours apart, are considered in the year. The DKR-ICF code gives the decay gamma source at different times following the final shot in the year. The adjoint dose field is then determined by performing a gamma adjoint calculation using the ONEDANT code with the flux-to-dose conversion factors representing the source at the point where the dose is to be calculated. The decay gamma source and the adjoint dose field are then combined to determine the biological dose rate at different times following shutdown. The contact dose at the outer surface of the borated layer was determined. In this case the borated water remains in place after shutdown. The dose rate was also calculated at a distance of 1.0 m outside the chamber wall for both cases with and without the borated water shield. Both the composition and trace elements of all materials used in the calculations except for the modified Al 5083 are taken from Ref. 5.6. The constituents of the low activation Al 5083^[5.7] are, by weight percent: 4.5% Mg, 94.99% Al, 0.5% Si and 0.01% Fe.

The different biological dose rates were calculated as a function of time following shutdown for the 2 1/4 Cr-1 Mo, Al 6061-T6 and low activation Al 5083 target chambers. Using the DKR-ICF code allows for appropriate modeling of the pulse sequence in ICF chambers. Figure 5.2 gives a comparison between the dose rates calculated for the steel chamber using the

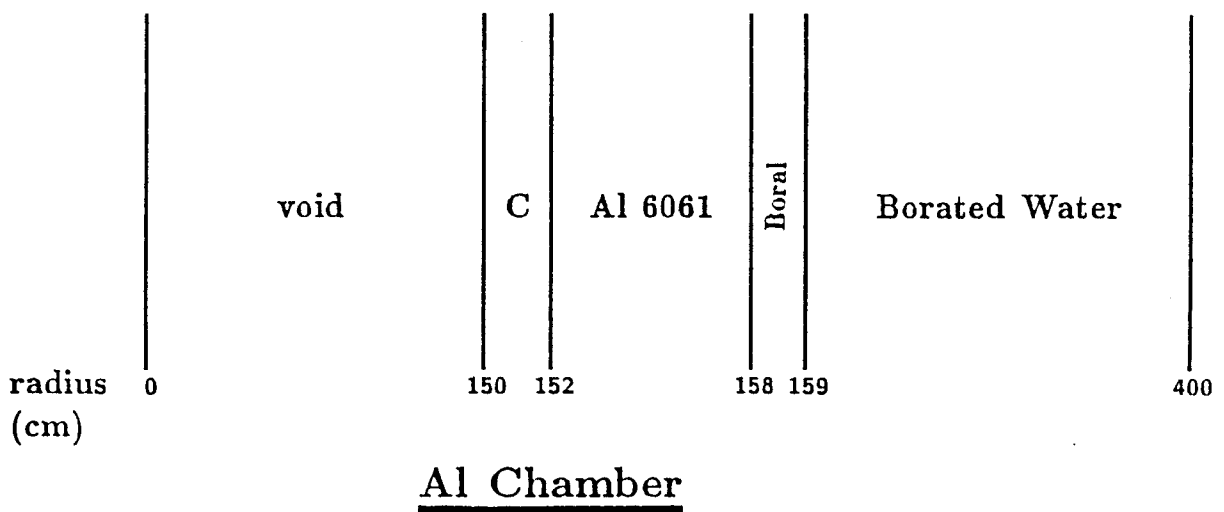
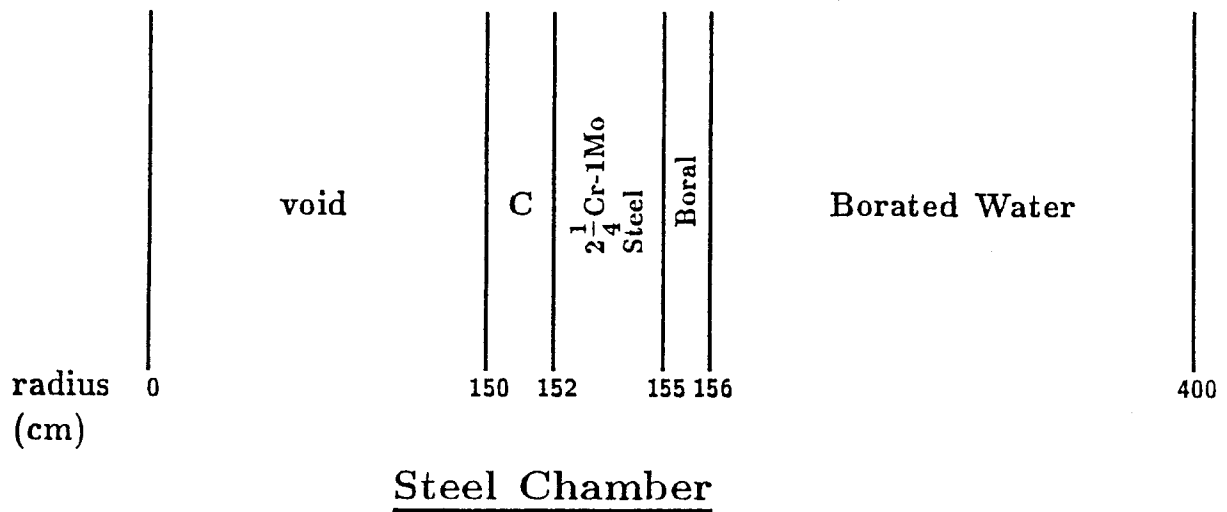


Fig. 5.1. Schematic of the chamber models used in the calculations.

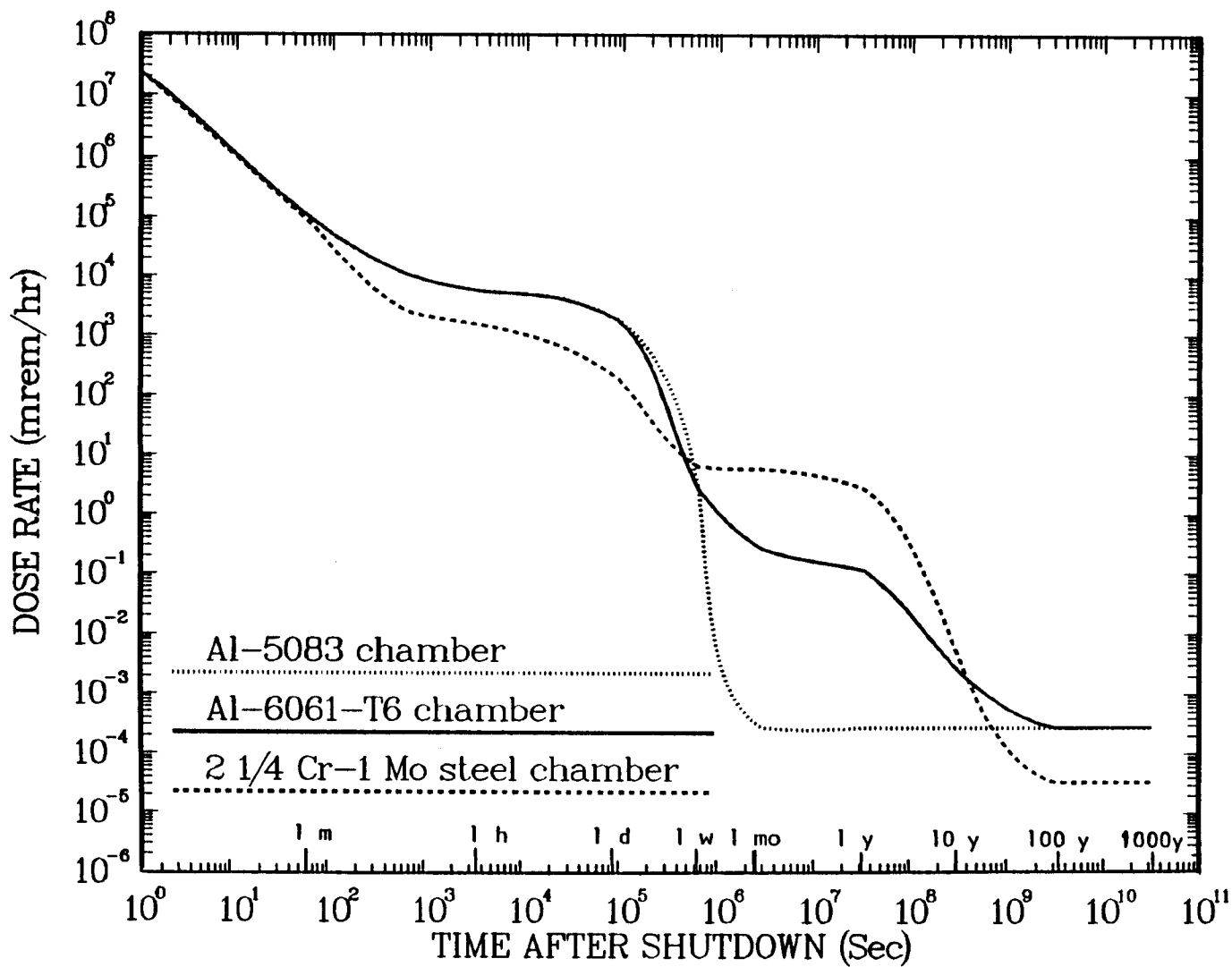


Fig. 5.2. Comparison between pulsed and steady state dose rates at the back of the 2 1/4 Cr - 1 Mo steel chamber.

pulse sequence and those obtained by assuming an equivalent steady state operation. Using the steady state operation results in underestimating the dose rate at shutdown by several orders of magnitude with the difference being negligible only after about one week following shutdown. The large difference within a short period of time following shutdown is due to the fact that the activity is dominated by short-lived radionuclides whose activities are sensitive to the operational schedule prior to shutdown due to buildup during the on-time with subsequent decay between periods of operation. Notice that the average neutron flux used in the equivalent steady state calculation is lower than that during the on-time preceding shutdown. On the other hand, the long term activity is dominated by long-lived radionuclides whose activity is determined by the total neutron fluence regardless of the temporal variation of the flux.

In both cases of the aluminum walls, the dose rate within the first 10 minutes following shutdown is dominated by ^{26}Na ($T_{1/2} = 1.07$ s) induced from ^{26}Mg (n, p), ^{27}Mg ($T_{1/2} = 9.45$ min) produced from ^{26}Mg (n, γ), ^{27}Al (n,p) and ^{30}Si (n, α), ^{28}Al ($T_{1/2} = 2.24$ min) produced from ^{27}Al (n,p) and ^{28}Si (n, γ), and ^{24}Na ($T_{1/2} = 15.02$ hr) induced from ^{23}Na (n, γ), ^{24}Mg (n,p) and ^{27}Al (n, α) reactions. The main contributor to the level of dose rate up to a week following shutdown is ^{24}Na . The dominant radionuclides in the Al 6061-T6 chamber between 1 week and 10 years are ^{54}Mn ($T_{1/2} = 313$ day) and ^{60}Co ($T_{1/2} = 5.27$ yr). While ^{54}Mn is produced from both ^{54}Fe (n,p) and ^{55}Mn (n,2n) reactions, ^{60}Co is mainly induced from the ^{60}Ni (n,p) reaction. The only major contributor to the dose rate in the same period of time for the low activation Al 5083 wall is ^{26}Al ($T_{1/2} = 7.3 \times 10^5$ yr) produced from ^{27}Al (n,2n). At times beyond 10 years after shutdown, the dose rate resulting from any of the two aluminum target chambers is due to ^{26}Al . The dominating radionuclides, except ^{60}Co , are all induced from the constituent elements, namely magnesium, aluminum and silicon in both the aluminum cases, in addition to manganese in the case of the Al 6061-T6 chamber. The radionuclide ^{60}Co is due to the impurity element nickel which is a trace element in both iron (60 wppm) and chromium (3 wppm), which is a constituent element of Al 6061-T6 only.

In the case of the steel chamber, the dose rate in the first few minutes following shutdown is

dominated by ^{28}Al , ^{56}Mn ($T_{1/2} = 2.6$ hr) induced from ^{55}Mn (n, γ) and ^{56}Fe (n,p), and ^{52}V ($T_{1/2} = 3.76$ min) produced from ^{51}V (n, γ), ^{52}Cr (n,p) and ^{55}Mn (n, α) reactions. The high content of manganese in the 2 1/4 Cr-1 Mo steel chamber, results in ^{56}Mn being the major contributor to the dose rate up to one day. In the period between 1 day and 10 years, as in the case of the Al 6061-T6 chamber, ^{54}Mn and ^{60}Co dominate the dose rate produced in the steel chamber. Beyond ten years after shutdown, the dose rate is primarily dominated by radionuclides induced from steel impurities. The two major contributors are ^{94}Nb ($T_{1/2} = 20,000$ yr) induced from ^{93}Nb (n, γ) and ^{94}Mo (n,p), and ^{93}Mo ($T_{1/2} = 3500$ yr) produced from ^{92}Mo (n, γ) and ^{94}Mo (n,2n) reactions.

Figure 5.3 compares the contact dose rate at the outer surface of the Al 6061-T6 chamber with the dose rate at 1 m distance from the chamber. It is clear that a reduction in dose rate is achieved by limiting access for maintenance to a distance larger than 1.0 m from the chamber. If the borated water is drained out after shutdown, the dose rate is reduced by a factor of 2-3 in the period between 1 day and 1 week after shutdown and the dose rate will drop below 100 mrem/hr if one waits for only two weeks after shutdown. If the borated water shield is left in place after shutdown, much lower dose rates will be obtained at all times except immediately after shutdown due to the ^{16}N ($T_{1/2} = 7.1$ s) produced from the activation of ^{16}O in the borated water. In this case the dose rate drops to 100 mrem/hr after three days and to only 2.7 mrem/hr in one week following shutdown.

A comparison between the different contact dose rates for the three alloys considered is shown in Fig. 5.4. The large amount of ^{24}Na produced in both aluminum chambers results in higher contact dose rates than the steel chamber up to approximately 3 days after shutdown. A significant drop in the aluminum chambers' dose rate levels occurs after about one day due to the decay of ^{24}Na . This results in the steel dose being at least an order of magnitude higher than the Al 6061-T6 dose over the period between 1 week and 5 years due to its higher content of ^{54}Mn . The contact dose rate level in the low activation Al 5083 chamber drops to a level which is three

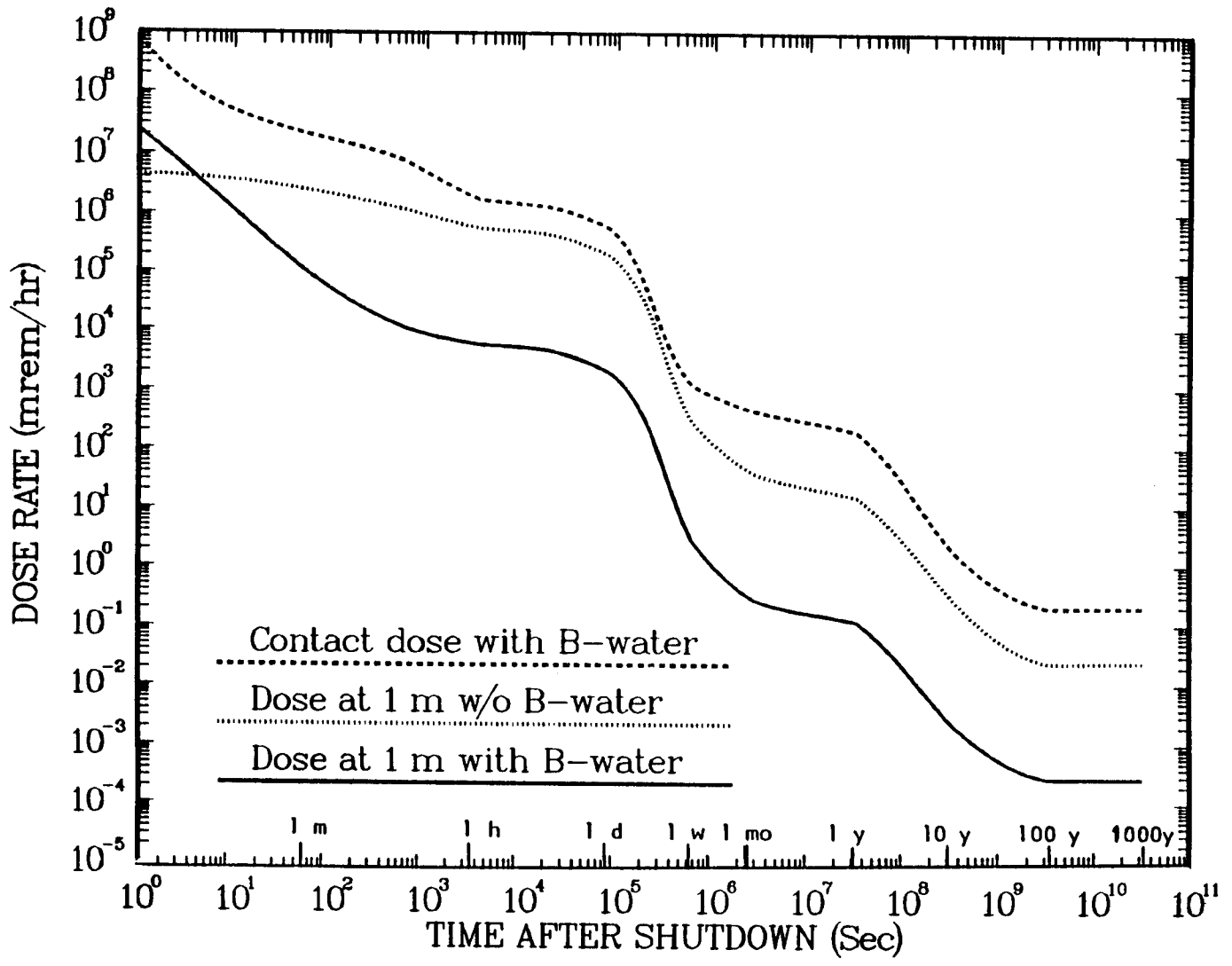


Fig. 5.3. Comparison between dose rates at the back of the Al 6061-T6 chamber and at a distance of 1 m from the chamber.

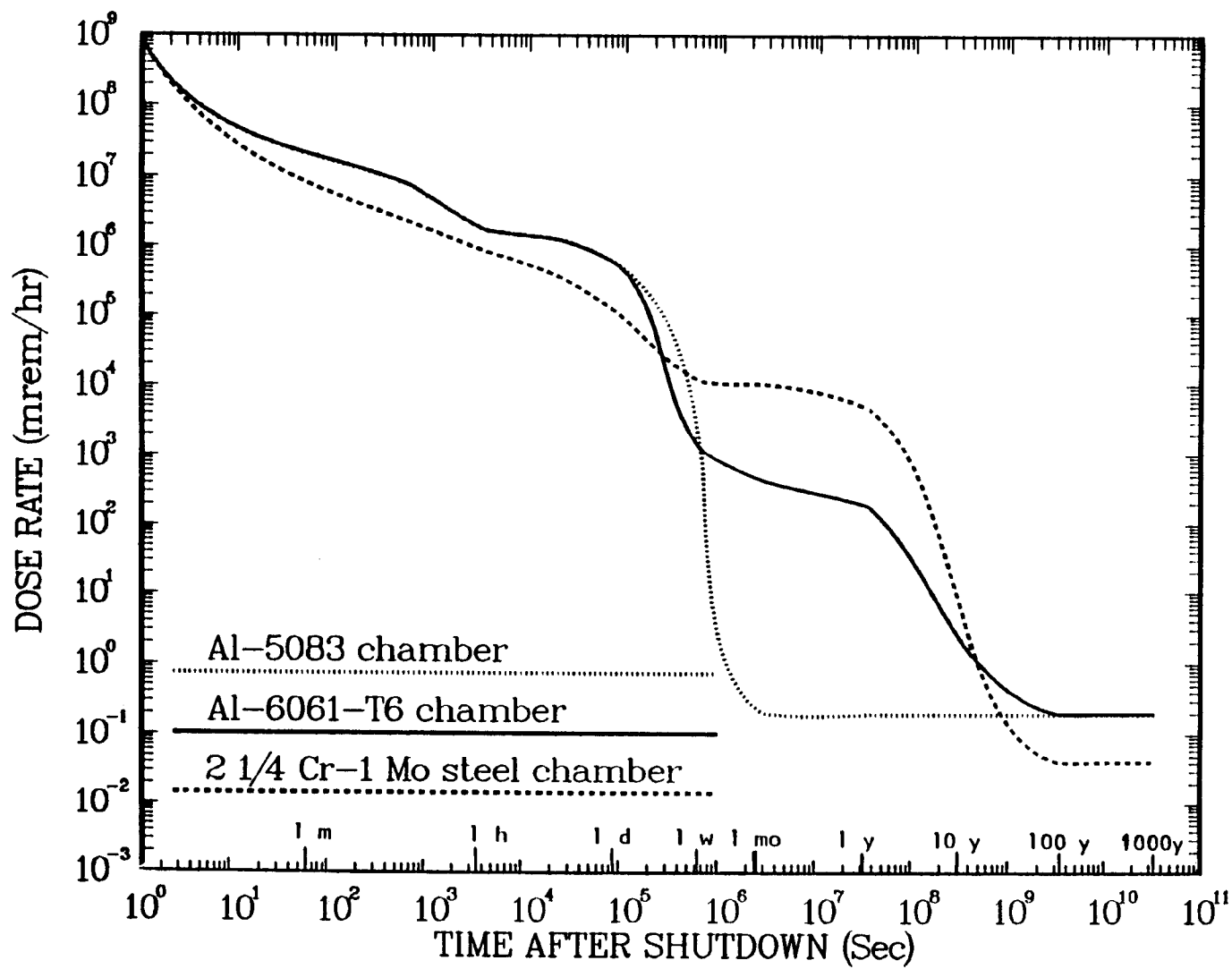


Fig. 5.4. Comparison between contact dose rates behind the chamber.

orders of magnitude less than the Al 6061-T6 and five orders of magnitude less than the 2 1/4 Cr-1 Mo dose rates within a couple of weeks following shutdown. Such a sharp drop in the dose level is due to the fact that the composition of the modified Al 5083 alloy used in these calculations does not contain most of the major constituent elements or impurities that produce any of the intermediate or long-lived radionuclides. Figures 5.5 and 5.6 show comparisons between the different dose rates at a distance 1.0 m from the surface of the target chamber with and without the borated water shield. Note that the results presented in Figures 5.4 and 5.5 are based on the assumption that the borated water shield will remain in place after shutdown and therefore represent the biological dose rate a diver would receive at the positions considered.

Table 5.1 lists the target chamber dose rate results obtained for the three different cases considered. The results show that due to the high level of the contact dose rate, no hands-on maintenance is possible within the first few years if either 2 1/4 Cr-1 Mo or Al 6061-T6 alloys were used as chamber wall materials. Using low activation Al 5083 allows for hands-on maintenance in 2-3 weeks following shutdown. If hands-on maintenance is limited to a distance greater than 1.0 m from the chamber, maintenance may start within days for the three alloys if the borated water is kept in place. If the borated water is drained out, maintenance can start after a week for the Al 5083 chamber and two weeks for the Al 6061-T6 chamber. On the other hand, hands-on maintenance for a 2 1/4 Cr-1 Mo steel chamber seems out of reach as the dose rate produced needs several years to cool down to a tolerable level. One should note that the results in Table 5.1 are given for 500 pulses each having the average yield of 200 MJ. As pointed out before, the dose in the first few days after shutdown is dominated by the short-lived radionuclides ^{24}Na ($T_{1/2} = 15.02$ hr) for the two aluminum cases and ^{56}Mn ($T_{1/2} = 2.6$ hr) for the steel case. The activity levels for these nuclides after shutdown are determined only by the last few pulses before shutdown. The yield for these pulses has to be used to give a proper estimate of the dose in the first few days following shutdown. The worst case estimate can be obtained by multiplying the results in the table for $t \leq 1$ day by 5 to account for the possibility of having the last few pulses at a yield of 1000 MJ. On the other hand, after a few days following shutdown, the dose is dominated

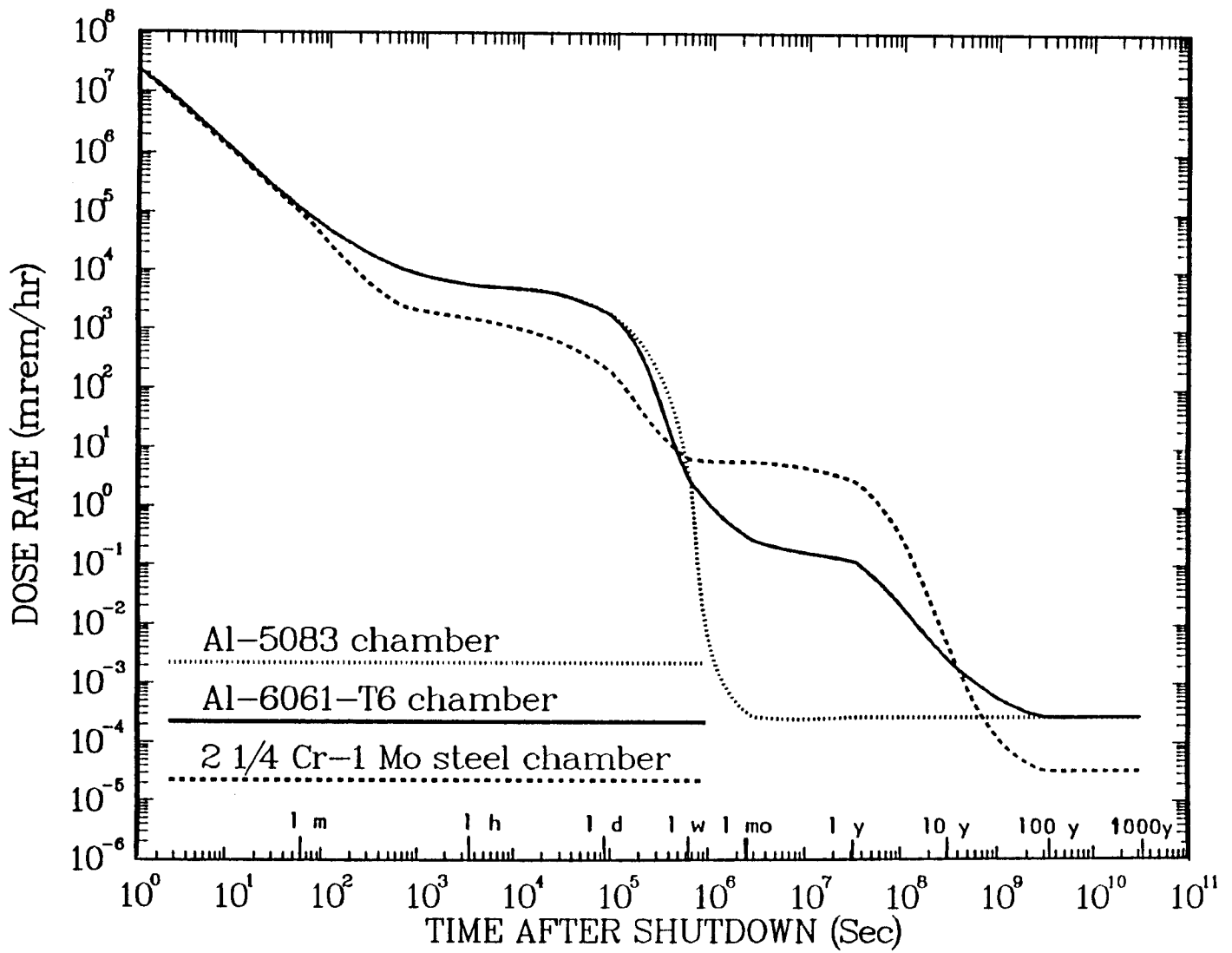


Fig. 5.5. Comparison between dose rates at a distance of 1 m from the chamber with borated water.

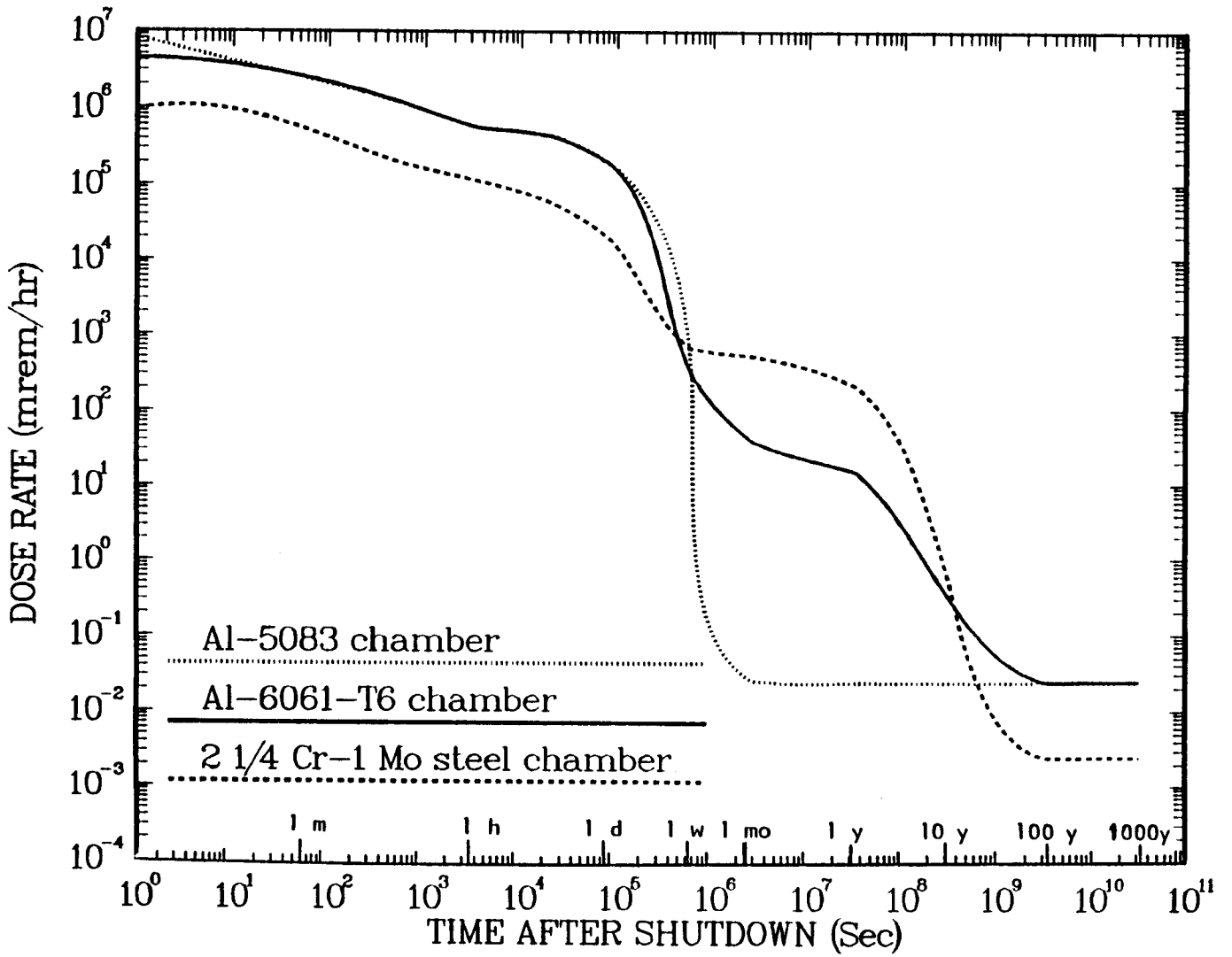


Fig. 5.6. Comparison between dose rates at a distance of 1 m from the chamber without borated water.

Table 5.1. Dose Rate (mrem/hr) Results for One Year Operation with 500 Shots and Average Yield of 200 MJ

Time After Shutdown	Contact Dose Rate				Dose Rate at 1 m (borated water drained out)		Dose Rate at 1 m (borated water in place)	
	$2\frac{1}{4}$ Cr-1Mo Steel	Al 6061-T6	Modified Al 5083	$2\frac{1}{4}$ Cr-1Mo Steel	Al 6061-T6	Modified Al 5083	$2\frac{1}{4}$ Cr-1Mo Steel	Al 6061-T6 Modified Al 5083
At shutdown	8.51×10^8	8.53×10^8	8.31×10^8	9.35×10^5	4.35×10^6	8.41×10^6	2.36×10^7	2.36×10^7
1 min	7.47×10^6	2.01×10^7	1.95×10^7	5.16×10^5	2.43×10^6	2.36×10^6	7.53×10^4	9.39×10^4
1 hr	8.5×10^5	1.73×10^6	1.73×10^6	1.11×10^5	5.5×10^5	5.5×10^5	1.5×10^3	5.58×10^3
1 day	1.04×10^5	5.4×10^5	5.4×10^5	1.84×10^4	1.84×10^5	1.84×10^5	2.02×10^2	1.88×10^3
1 week	1.16×10^4	1.19×10^3	6.95×10^2	6.57×10^2	2.82×10^2	2.37×10^2	6.62	2.7
1 month	1.07×10^4	4.45×10^2	0.204	5.17×10^2	38.9	2.52×10^{-2}	5.95	0.28
1 year	4.95×10^3	1.91×10^2	0.2	2.06×10^2	15.02	2.37×10^{-2}	2.77	0.12
10 years	4.66	1.92	0.196	0.407	0.28	2.35×10^{-2}	3.48×10^{-3}	2.31×10^{-3}
Time for dose rate <100 mrem/hr	5 yr	1.5 yr	2 wk	3 yr	2 wk	1 wk	3 d	3 d
Time for dose rate <2.5 mrem/hr	10 yr	7.5 yr	3 wk	8 yr	3 yr	10 d	1 yr	1 wk

by the relatively long-lived radionuclides ^{54}Mn ($T_{1/2} = 313$ day) and ^{60}Co ($t_{1/2} = 5.27$ yr). All shots during the year operation period will contribute to the activity of these radionuclides. Hence, for a proper estimate of the dose rate in this period, the detailed temporal distribution of the different yield shots is required.

References for Section 5

- 5.1. R. O'Dell, et al., "User's Manual for ONEDANT: A Code Package for One-Dimensional, Diffusion-Accelerated, Neutral Particle Transport," LA-9184-M, Los Alamos National Laboratory, 1982.
- 5.2. R. MacFarlane, "Nuclear Data Libraries from Los Alamos for Fusion Neutronics Calculations," *Trans. of ANS*, Vol. 46, pp. 271-272, 1984.
- 5.3. M. Sawan, et al., "Nuclear Analysis of the Heavy-Ion-Beam-Driven Fusion Reactor HIBALL," *Nuclear Technology/Fusion*, Vol. 4, pp. 79-92, July 1983.
- 5.4. D. L. Henderson and O. Yasar, "DKR-ICF: A Radioactivity and Dose Rate Calculation Code Package," Vol. 1, University of Wisconsin Fusion Technology Institute Report UWFD-714, April 1987.
- 5.5. M. A. Gardner and R. J. Howerton, "ACTL: Evaluated Neutron Activation Cross Section Library - Evaluation Techniques and Reaction Index," UCRL-50400, Vol. 18, Lawrence Livermore National Laboratory, 1978.
- 5.6. D. Henderson, M. Sawan and G. Moses, "Radiological Dose Calculations for the Diode Region of the Light Ion Fusion Target Development Facility," *Fusion Technology*, Vol. 13, pp. 594-615, May 1988.
- 5.7. R. F. Bourque, et al., "Innovative Design Concepts for the LMF Target Chamber and Related Systems," GA-A19651, General Atomics, June 1989.

6. X-RAY VAPORIZATION EFFECTS

6.1. Introduction

The LMF would explode targets with yields of up to 1000 MJ at a rate of from one per week to two per day.^[6.1] In this study, these targets will be driven to implosion by light ion beams, which place limits on the density and type of the gas permitted in the target chamber. The current design calls for propagation of the ions in a ballistic mode that requires a 1 torr helium target chamber gas. Therefore, the x-rays generated by the burning target will pass through the target chamber gas and will deposit their energy in the target chamber wall. The pulse width of this burst of x-rays is typically a few nanoseconds, much shorter than the thermal diffusion time in the wall. The resultant energy densities are high enough to vaporize the inside layer of the wall, irrespective of the wall material. The vaporized wall material will be at pressures of from tens to hundreds of kbar,^[6.2] which is high enough to launch shocks into the unvaporized part of the wall material. These shocks can further damage the wall material or change its properties so that the response is different on subsequent shots.

Here results are reported of an attempt to experimentally test the response of some proposed target chamber wall materials to intense bursts of x-rays. The approach used in this study has been to use x-rays from a gas pinch source that have about the same photon energies as would x-rays emitted from an ICF target. The SATURN facility at Sandia National Laboratory in Albuquerque was used in this manner to provide x-ray fluences and intensities that are relevant to LMF conceptual designs. The LMF parameters are discussed for a few concepts and it will be shown how experiments on SATURN can indeed be relevant. Then experiments will be described and results will be presented and discussed. Finally additional work planned for the near future is identified.

6.2. Simulation of Experiments

A radiation-hydrodynamics code has been used to simulate the deposition of x-rays in the material. This calculation is then coupled to the CSQ computer code. CSQ is written and maintained at SNL which uses two-dimensional Eulerian hydrodynamics and has sophisticated modeling of phase transitions and crush physics that are probably important to shock attenuation in

materials.^[6.3] CSQ has rather limited radiation transport modeling, which makes such coupling to another computer code advisable when doing x-ray vaporization simulations.

CSQ was used to study how sample first wall materials might behave in experiments that mimic target chamber x-ray conditions. Such computer calculations were done for samples made of aluminum, aluminum coated with a thin layer of alumina and graphite. The parameters for three experimental environments are shown in Table 6.1 along with LMF conditions for SNL and LLNL concepts where the wall is assumed to be aluminum. The SNL target chamber designs are 1.5 m in radius while the LLNL design has a radius of 5.0 m. PROTO-II is an electron accelerator at SNL that has been used for a number of years to create pulses of x-rays with gas pinches.^[6.4] Specifically, gas puff pinches of neon produce the spectrum shown in Fig. 6.1.^[6.5] When one compares this spectrum with the HIBALL target spectrum,^[6.6] both have peaks at about 1 keV in photon energy. The experimental arrangement is shown in Fig. 6.2. The pinch is created in the center of a circle of current return posts and the closest that a sample can be placed to the x-ray source is just outside these posts. SATURN is a machine similar to PROTO-II at SNL except that it is much larger and only fired its first gas pinches in late 1988. Experiments on SATURN have a very similar arrangement to those in PROTO-II. GAMBLE-II is a machine at NRL that can accelerate protons in a beam to simulate x-ray deposition. One should note that the pulse width of the ion beam on GAMBLE-II is more than 40 ns while the gas pinch x-ray sources have less than half the pulse width. If one is only interested in stresses in the center of the material so that the energy density is important, then experiments on all three machines can be relevant to the LMF. If, however, stresses near the surface are important, the power density (power deposited per unit mass) is the important parameter and only SATURN can do LMF relevant experiments. Even SATURN can only provide a power at one half the LLNL LMF value. The bottom line is the achievable stress in the material, which was calculated with CSQ for PROTO-II, SATURN, and SNL and LLNL versions of the LMF. In aluminum, PROTO-II can provide stresses of 1 GPa 0.05 cm in back of the first surface and SATURN can provide 7.5 GPa. The stresses that

Table 5.1. Dose Rate (mrem/hr) Results for One Year Operation with 500 Shots and Average Yield of 200 MJ

Time After Shutdown	Contact Dose Rate				Dose Rate at 1 m (borated water drained out)		Dose Rate at 1 m (borated water in place)	
	$2\frac{1}{4}$ Cr-1Mo Steel	Al 6061-T6	Modified Al 5083	$2\frac{1}{4}$ Cr-1Mo Steel	Al 6061-T6	Modified Al 5083	$2\frac{1}{4}$ Cr-1Mo Steel	Al 6061-T6 Modified Al 5083
At shutdown	8.51×10^8	8.53×10^8	8.31×10^8	9.35×10^5	4.35×10^6	8.41×10^6	2.36×10^7	2.36×10^7
1 min	7.47×10^6	2.01×10^7	1.95×10^7	5.16×10^5	2.43×10^6	2.36×10^6	7.53×10^4	9.39×10^4
1 hr	8.5×10^5	1.73×10^6	1.73×10^6	1.11×10^5	5.5×10^5	5.5×10^5	1.5×10^3	5.58×10^3
1 day	1.04×10^5	5.4×10^5	5.4×10^5	1.84×10^4	1.84×10^5	1.84×10^5	2.02×10^2	1.88×10^3
1 week	1.16×10^4	1.19×10^3	6.95×10^2	6.57×10^2	2.82×10^2	2.37×10^2	6.62	2.7
1 month	1.07×10^4	4.45×10^2	0.204	5.17×10^2	38.9	2.52×10^{-2}	5.95	0.28
1 year	4.95×10^3	1.91×10^2	0.2	2.06×10^2	15.02	2.37×10^{-2}	2.77	0.12
10 years	4.66	1.92	0.196	0.407	0.28	2.35×10^{-2}	3.48×10^{-3}	2.31×10^{-3}
Time for dose rate <100 mrem/hr	5 yr	1.5 yr	2 wk	3 yr	2 wk	1 wk	3 d	3 d
Time for dose rate <2.5 mrem/hr	10 yr	7.5 yr	3 wk	8 yr	3 yr	10 d	1 yr	1 wk

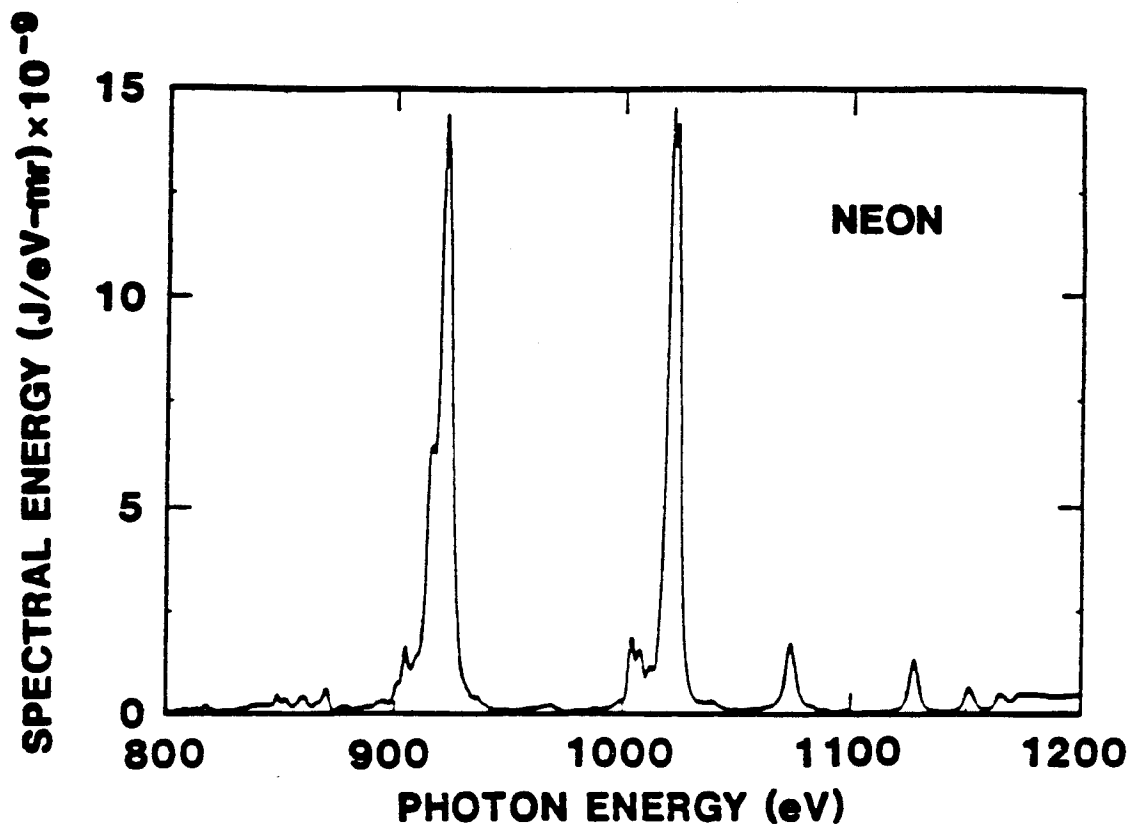


Fig. 6.1. X-ray spectrum from a neon gas pinch on PROTO-II. Only the component above 900 eV in photon energy is shown. There is another component to the spectrum below a few hundred eV that has about 4 times the energy but more than 5 times the pulse width.

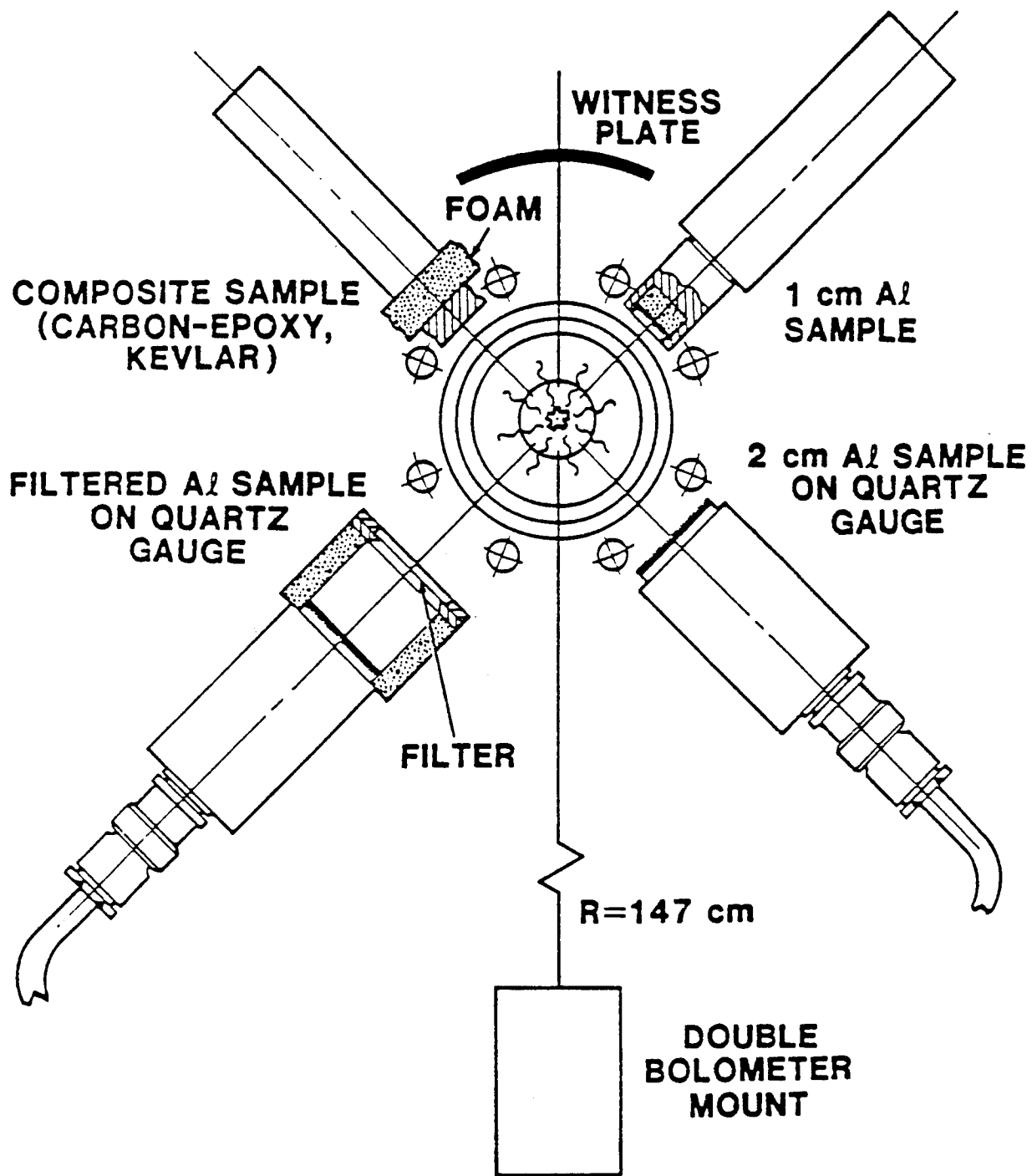


Fig. 6.2. Schematic picture of experimental arrangement in PROTO-II.

GAMBLE-II could generate in aluminum have not been calculated, though based on the power density one would expect about 1 GPa. The stresses in a LLNL and SNL LMF aluminum wall were calculated to be 7.5 GPa and 14.0 GPa, respectively. The calculation of the PROTO-II stresses was rather interesting because here the stresses are only a factor of a few larger than the yield stress and the stresses are anisotropic. The longitudinal stresses at 0.05 cm peaked at 1.0 GPa while the transverse stresses peaked at 0.7 GPa. These simulations show that experiments on SATURN have the potential to much more closely mimic the conditions in the LMF target chamber than do experiments on GAMBLE-II or PROTO-II.

The response of four different materials to x-rays from SATURN has been simulated with CSQ. The results are summarized in Table 6.2. In all cases, the samples are assumed to be 3.8 cm from the pinch, which is assumed to generate 100 kJ of x-rays in the lines shown in Fig. 6.1. There is assumed to be another 400 kJ in x-rays below about 200 eV in photon energy, making a total of 500 kJ in x-rays. It is assumed that the x-rays above 900 eV are emitted in 20 ns in these simulations and that the low energy component is radiated over 100 ns. Simulations for aluminum, graphite and aluminum coated with a 100 micron thick layer of alumina have been carried out.

The effects of these low energy photons have been considered. Simulations have been done where these photons are filtered out, perhaps with an aluminum foil, and where they are allowed to irradiate the sample. The ranges of 200 eV x-rays in aluminum and alumina are more than an order of magnitude less than the ranges of 1 keV x-rays and should be mostly absorbed in the blowoff plasma and not contribute to the launching of a shock in the material. Therefore, only results are shown for these materials where the low energy photons have not been filtered out; the results with filtering are essentially the same. This is not the case for graphite because the range of 200 eV x-rays is only a little shorter than that for 1 keV x-rays. Both unfiltered and filtered simulations are shown for graphite.

Table 6.2. Stresses in Various Materials Generated with SATURN X-rays

	Aluminum (unfiltered)	Graphite (unfiltered)	Graphite filtered)	Alumina/Aluminum (unfiltered)
Range of 1 keV X-rays (mg/cm ²)	0.83	0.50 ⁽¹⁾	0.50	0.38
Mass Density (g/cm ³)	2.7	1.7	1.7	3.5
Energy Fluence (J/cm ²)	550 ⁽²⁾	2750	550	550 ⁽²⁾
Energy Density (kJ/g)	660	5500	1100	1440
Power Density (GW/g)	44	367	73	96
Calculated Stress @ 0.05 cm (GPa)	7.5	36.0	10.2	3.5
Calculated Stress @ 0.25 cm (GPa)	4.8	12.5	5.0	1.8
Calculated Stress @ 0.25 cm (GPa)	2.7	8.0	N.A.	1.0

(1) The ranges of 1 keV and 300 eV x-rays in carbon are the same. The range of 100 eV x-rays is 0.05 mg/cm².

(2) Because of the much shorter range of low energy photons, the part of the spectrum below 900 eV is ignored and is not included in the energy fluence.

6.3. Experiments on SATURN

During May, 1989, some x-ray vaporization experiments were fielded on SATURN like those described in the previous section. All of the samples were donated by LLNL or SNL. The space on the machine was just what remained on experiments which were already planned. The exception to this was shot 669 which had only outside samples on it and was donated by SNL. There were no active diagnostics to measure the stress levels. The sample holders were loaned by other experimenters at SNL. Stainless steel Swagelok fittings held the samples in place with an annular lip. The backs of the samples were supported with carbon foam that was, in turn, supported with a thin aluminum disk. Results of these experiments are still being analyzed but preliminary findings are presented in Table 6.3. A photograph of the samples after they were irradiated is shown in Fig. 6.3. One can see in Table 6.3 that all samples except 2 and 5 were utterly destroyed. Sample 5, a two-directionally woven graphite in a carbon matrix called K-Karb, was not damaged in the plane of the graphite fibers but these planes became delaminated. A closeup photograph of Sample 5 is shown in Fig. 6.4. Sample 2, shown in Fig. 6.5, is aluminum 6061-T6 with a layer of alumina deposited on its surface. It survived well except that the alumina was removed. All of the other samples were fine grained graphites or graphites with short fibers. Sample 3, Graphnol, was a fine grained graphite that survived the best of these as it was broken into about 6 pieces. The others were turned into powder. No pieces of sample 4 could be found.

In August of 1989, another set of experiments was fielded on SATURN. The samples are shown in Fig. 6.6 after they were shot. These used argon gas pinches as an x-ray source. The spectra from these pinches differ from those for neon in the photon energy of the dominant lines; neon has lines at about 0.9 and 1.0 keV, while argon emits lines in the 3 to 4 keV range. Also, argon has about 40 kJ in these lines, while neon can have as much as 100 kJ in its lines. The pulse widths of the x-rays can be as low as 10 ns for argon gas pinches. For these experiments, the samples were three and four directionally woven graphites in a solid carbon matrix, bare aluminum 6061 and aluminum 6061-T6 coated with a layer of carbon, a loose carpet material made

SATURN Irradiated LMF First Wall Sample Materials

(x-rays from Neon gas pinches)

Graphite
H-451



Al 6061
coated with Alumina



Graphite
Graphnol N3M



Graphite
A05

(nothing left)

Graphite
K-Karb
(2-D weave)



Graphite
CGW



Graphite
ATJ



Graphite
Dunlop breakpad



TYPICAL PARAMETERS

Spectrum - 1 keV lines

Fluence - 500 J/cm²

Pulse Width - 15 to 20 ns

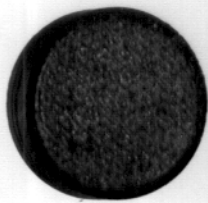


SAMPLE HOLDER



Fig. 6.3. Photograph of eight samples shot on SATURN May 1989 with a neon gas puff.

SATURN Irradiated 2-D Woven Graphite



Neon Gas Puff

Spectrum ~ 1 keV lines
+ blackbody
Line Fluence 730 J/cm^2
Total Fluence 3400 J/cm^2
Pulse Width 16 ns

 University of
Wisconsin



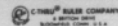
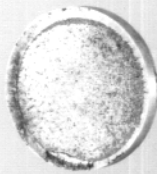
No. 18 

Fig. 6.4. Photograph of K-Karb after irradiation on SATURN.

**SATURN Irradiated Aluminum
Coated with Alumina**



Neon Gas Puff

Spectrum	~1 keV lines + blackbody
Line Fluence	390 J/cm ²
Total Fluence	1900 J/cm ²
Pulse Width	21 ns

 University of
Wisconsin

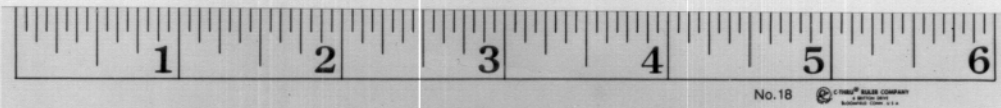


Fig. 6.5. Photograph of aluminum coated with alumina after irradiation on SATURN.

**SATURN Irradiated LMF First Wall Sample Materials
X-rays from Gas Pinches**

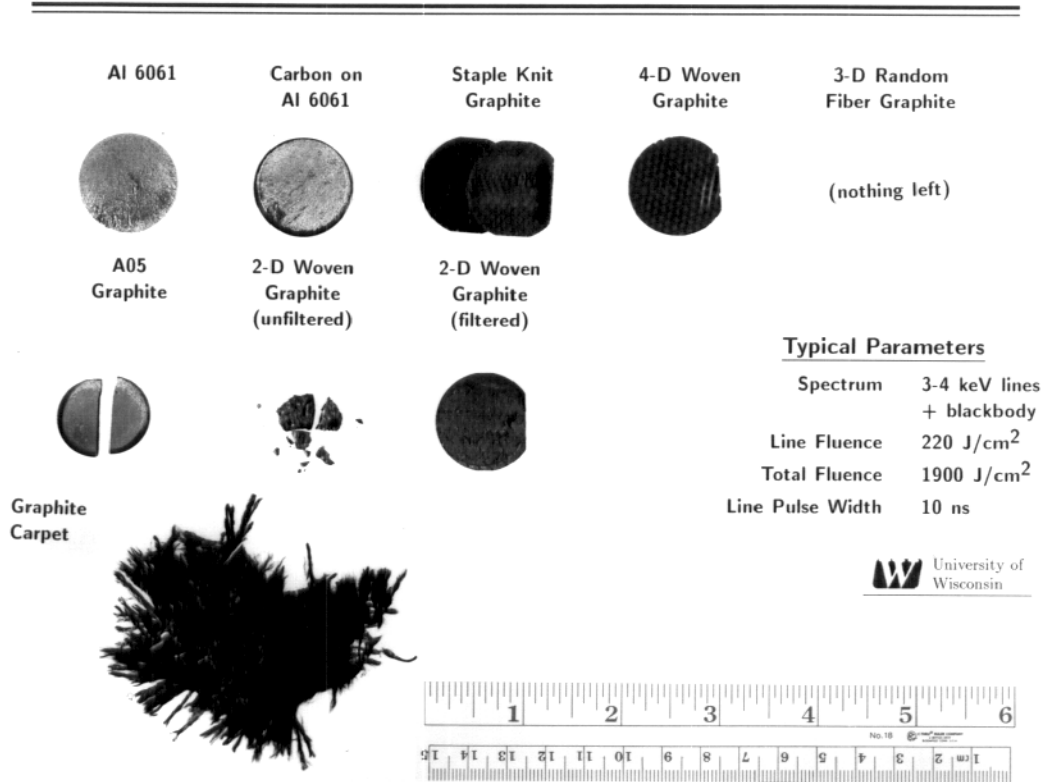


Fig. 6.6. Photograph of samples after irradiation on SATURN August 1989 with an argon gas puff.

Table 6.3. Samples of LMF First Wall Materials Irradiated with SATURN X-Rays in May 1989

Sample No.	Shot No.	Material	Result
1	658	Graphite H-451 fine grained	Destroyed, powder
2	658	Alumina coated aluminum 6061-T6	Survived
3	664	Graphnol fine grained graphite	Destroyed, six pieces
4	665	Graphite AO5 short random fibers in a carbon matrix	Destroyed, nothing left
5	669	K-Karb 2-D woven graphite in a carbon matrix	Survived, delaminated
6	669	Graphite CGW fine grained	Destroyed, powder
7	669	Graphite AJT fine grained	Destroyed, powder
8	669	Dunlop breakpad graphite fibers in a carbon matrix	Destroyed, shredded

of graphite, and two samples of two-directionally woven graphite, where the x-rays were unfiltered and then filtered with a thin aluminum foil. The three and four directional graphites were an attempt to stop the delamination seen in K-Karb. The aluminum experiments are an extension of the previous experiments with alumina on aluminum in that they use a sacrificial layer to protect the aluminum, while carbon would be much easier to spray onto the wall of an LMF before each shot. The carbon carpet is a relatively new idea for LMF target chamber wall protection,^[6,7] which uses the looseness of a long fibered carpet to prevent the generation of a shock. The filtering of x-rays is an experimental test of the low energy photon effects examined computationally.

The results of these experiments are given in Table 6.4. One can see that the aluminum survived both with and without the carbon protection. The four-directional weave was successful in combating delamination, though the three-directional random weave was not. The graphite carpet was almost totally undamaged by x-rays. The unfiltered two-directional weave was destroyed, while the filtered sample survived. There are no quantitative results yet as to the performance of the gas pinches, but preliminary indications are that there were in excess of 350 kJ of x-rays on all

shots.

Table 6.4. Samples of LMF First Wall Materials Irradiated with SATURN X-rays in August 1989

Sample No.	Shot No.	Material	Result
1	736	Bare Aluminum 6061-T6	Survived
2	736	Carbon Coated Aluminum 6061-T6	Survived
3	736	Stapleknit graphite	Destroyed, delaminated
4	737	4-D Woven Graphite (FMI)	Survived
5	739	3-D Random Fiber Graphite	Destroyed
6	737	AO5 Graphite Fine Grained	Survived
7A	739	2-D Woven Graphite (Unfiltered)	Destroyed
7B	739	2-D Woven Graphite (Filtered)	Survived
8	737	Graphite Carpet	Survived

6.4. Summary and Future Work

The experiments reported here show that woven graphites and aluminum with a protective layer of alumina survived LMF relevant x-ray pulses. Three types of graphite with fibers in three or four directions were irradiated and it was found that 4-D woven survives x-rays from an argon pinch. Bare aluminum and aluminum coated with a thin layer of graphite were tested in a beam of argon pinch x-rays and it was found that both survived. Carbon carpet also survived such testing. It was computationally and experimentally shown that filtering of the low energy photons in the pinch spectrum makes a great difference to the response of graphites.

Additional analysis of the experiments is planned. Once all of the data is resolved, CSQ will be used to simulate the response of the sample materials for the spectrum observed in the experiment. Samples are also being analyzed to look for changes in the microstructure induced by

the x-ray driven shocks. Hardness changes of the irradiated materials will also be measured.

Additional experiments on SATURN are planned. The experiments in Table 6.4 will be repeated for neon pinch spectra to test the effects of spectrum. Some samples will be repetitively tested since that is what they will experience in the LMF. Other materials which may be more relevant to ICF power reactors will also be tested.

References for Section 6

- 6.1. U.S. Department of Energy Inertial Fusion Division, "LMF-Laboratory Microfusion Capability Study, Phase I Summary," DOE/DP-0069.
- 6.2. B. Badger, et al., "Target Chamber Studies for a Light Ion Fusion Laboratory Microfusion Facility," University of Wisconsin Fusion Technology Institute Report UWFDI-768, August 1988.
- 6.3. S.L. Thompson and J.M. McGlaun, "CSQIII, An Eulerian Finite Difference Program for Two-Dimensional Material Response: Users Manual," Sandia National Laboratories Report SAND87-2763, January 1988.
- 6.4. R.B. Spielman, et al., "Z-Pinch Experiments on SATURN at 30 TW," 2nd International Conference on Dense Z-Pinch, April 26-29, 1989, Laguna Beach, CA, AIP Conference Proceedings, Vol. 195, pp. 3-16, 1989.
- 6.5. "Progress Report: Narya Pulsed-Power-Driven X-Ray Laser Program--January 1984 through June 1985," M.K. Matzen, ed., SAND85-1151, Sandia National Laboratories, 1986.
- 6.6. G.A. Moses, R.R. Peterson, M.E. Sawan and W.F. Vogelsang, "High Gain Target Spectra and Energy Partitioning for Ion Beam Reactor Design Studies," University of Wisconsin Fusion Technology Institute Report UWFDI-396, November 1980.
- 6.7. M.J. Monsler and W.R. Meier, "A Carbon Carpet First Wall for the Laboratory Microfusion Facility," *Fusion Technology*, Vol. 15, pp. 595-602, 1989.

7. X-RAY DRIVEN FRAGMENTATION

A topic related to x-ray vaporization of first wall material is x-ray generated fragmentation of other structures in target chambers and the acceleration of such fragments into shrapnel. Some analytic models of fragmentation have been coupled with an x-ray generated shock formalism to develop a means of estimating the size and speed of the shrapnel fragments. Shrapnel parameters were then estimated for two types of structures that could be in the target chamber. The effects of the resulting shrapnel on the target chamber wall have not yet been estimated.

Fragmentation was considered as a two step process: 1) x-rays generate a large pressure gradient in the material which causes the material to move, and 2) this motion provides kinetic energy, some of which can be converted into the surface energy required for fragmentation. Step 1 can be modeled by a simple energy per volume method. For step 2, the methods of Grady [7.1] were used.

It was found that, as long as the deposition length is less than $C_s dt$, where C_s is the speed of sound in the unvaporized material and dt is the width of the x-ray pulse, the pressure is proportional to $\sin \alpha$, where α is the angle between the incident x-rays and the surface of the material. For graphite, it was found by comparison with computer simulations and experiment that the pressure from an x-ray intensity of I_x is

$$P = 0.38 I_x \sin \alpha / C_s \quad (7.1)$$

of momentum. If the thickness of the material is T and the mass density is r , its areal mass density is ρT . The impulse is $P \Delta t$, which is the momentum gained by the material. Therefore, the velocity of the material is independent of the size of fragments it is broken into and can be expressed as

$$v_{\text{frag}} = 0.38 I_x \sin \alpha \Delta t / \rho T . \quad (7.2)$$

Finally, the sizes of the fragments must be calculated. The Grady model allows some of the kinetic energy about the center of mass of a piece of material that is to become a fragment to be converted into the surface energy of the fragment. For a solid, this model predicts that the average diameter of a fragment is

$$d = 2.72 (K_{Ic}/r \dot{\epsilon} C_s)^{2/3} . \quad (7.3)$$

Here, K_{Ic} is the fracture toughness, which for graphite is between 3×10^8 and 3×10^9 dyne/cm^{3/2}. The larger value is more conservative because it will lead to larger, more damaging shrapnel.

This formalism was used to consider the fragmentation into shrapnel of two different structures. Both structures are assumed to be in an LMF target chamber where they are subjected to the x-rays from a 1000 MJ target microexplosion.

First a sphere of graphite concentric with the target was considered. For a sphere, α is 90° and the strain rate is

$$\dot{\epsilon} = 2 v_{frag}/3 R , \quad (7.4)$$

where R is the distance between the target inside of the graphite sphere. Therefore, we can write the fragment diameter as

$$d = 4.53 \times 10^{-7} R^2 T^{2/3} \text{ (cm)} . \quad (7.5)$$

Some results are tabulated in Table 7.1 for a graphite sphere, with $T = 0.1$ cm and for R from 10 to 100 cm. In addition to the fragment velocities and diameters, the fragment mass, M_{frag} , and momentum, Mom_{frag} , are listed. Notice that the momentum of each fragment increases with distance from the target.

Table 7.1. Fragment Parameters for a Sphere of Graphite Concentric with Targets in LMF Target Chamber

R (cm)	V _{frag} (m/s)	d (cm)	M _{frag} (g)	Mom _{frag} (g-cm/s)
10	2130	1.0x10 ⁻⁵	9.6x10 ⁻¹⁵	2.0x10 ⁻⁹
20	1070	3.9x10 ⁻⁵	5.8x10 ⁻¹³	6.2x10 ⁻⁸
50	430	2.4x10 ⁻⁴	1.3x10 ⁻¹⁰	5.6x10 ⁻⁶
100	213	1.0x10 ⁻³	9.6x10 ⁻⁹	2.0x10 ⁻⁴

The second structure considered was a hollow graphite cylinder pointed directly at the target. Here, $\sin \alpha$ is not constant, but is a function of the tube's radius and the distance that part of the tube is from the target,

$$\sin \alpha = r_{\text{tube}} / (r_{\text{tube}}^2 + R^2)^{1/2} . \quad (7.6)$$

It is assumed that the tube's radius, r_{tube} , is greater than the target radius, so that the target can be treated as a point source of x-rays. This insures that the x-rays will deposit on the inside surface of the tube and the tube will fragment due to rapid outward expansion. The pressure driving this expansion is, if $R \gg r_{\text{tube}}$,

$$P = 4.96 \times 10^7 r_{\text{tube}} / R^2 \text{ (MPa)} . \quad (7.7)$$

The velocity at which the tube cylindrically expands is

$$v_{\text{frag}} = 2.16 \times 10^5 r_{\text{tube}} / T R^2 \text{ (cm/s)} . \quad (7.8)$$

For a cylindrical expansion, the strain rate is

$$\dot{\epsilon} = v_{\text{frag}}/3 r_{\text{tube}} . \quad (7.9)$$

From the preceding equations, the fragment diameter is

$$d = 7.18 \times 10^{-3} T^{2/3} R^2 \text{ (cm)} . \quad (7.10)$$

For $r_{\text{tube}} = 1$ cm and $T = 0.01$ cm, the pressure, fragment speed, diameter, mass, and momentum are tabulated in Table 7.2. Once again, one will notice that the momentum of a fragment increases as the distance from the target. The fragment speed falls off rather quickly because of the variation in $\sin \alpha$.

Table 7.2. Fragment Parameters for Graphite Tube in LMF Target Chamber

R=	10 cm	20 cm	50 cm	100 cm	150 cm
P (GPa)	496	124	20	5.0	2.2
V_{frag} (m/s)	2160	540	86	22	9.6
d (cm)	0.033	0.133	0.833	*	*
M_{frag} (mg)	0.36	22.8	5578	*	*
Mom _{frag} (g-cm/s)	77	1232	4.8x10 ⁴	*	*

*Fragment sizes are so large that model is no longer valid

References for Section 7

- 7.1. D.E. Grady, "Local Inertial Effects in Dynamic Fragmentation," *J. Appl. Phys.*, Vol. 53, p. 322, 1982.

8. CONCLUSIONS

Several aspects of the target chamber for the LIB LMF have been studied. These have included x-ray driven x-ray vaporization, target chamber gas response, structural response and activation of the target chamber. Based on these studies, a target chamber has been designed consistent with ballistic ion beam transport and which will survive the lifetime of the facility.

This is part of a multiyear effort to study the LIB LMF and there are several issues which need more study. These include:

- 1) **Continued study into the physics of x-ray vaporization.** Better diagnostics on SATURN experiments will allow comparison of experiments with computer simulations on the basis of a shock strength at a given position in a material. More materials need to be experimented upon and the data base of material properties for thermal liner materials needs to be enlarged.
- 2) **Continued study into the behavior of target chamber gases.** The current estimates of the pressure loadings on the first wall are based on one-dimensional computer simulations, which should be augmented with two-dimensional and better one-dimensional simulations. Specifically, a long term history of the pressure on the wall is needed to accurately predict the wall structural response. Effects of recondensation of vaporized wall material and the flow of vapor up beam tubes need more consideration.
- 3) **Continued study into the structural response on the target chamber.** The use of finite-element codes will ultimately be required to analyze the effects of beam ports on the structural response. Better pressure loading results will require a recalculation of the mechanical response and estimated required wall thicknesses.
- 4) **Changes in the ion beam propagation physics.** If an ion beam microdivergence of 6 mrad cannot be achieved, either the target chamber radius must be reduced or the propagation scheme must be changed. In making this decision one should know whether a smaller target chamber is feasible or how much one would be required to lower the target yield to allow for a smaller target chamber.
- 5) **The target chamber must be consistent with the expected uses of the LMF.** Weapons effects simulation experiments are to be performed in the LMF. It is not yet known whether

the current target chamber design is of proper geometry to allow these experiments. Also, it is not known how the experiments will affect the survival of the target chamber. Another aspect of this issue is that the experiments must be carried out in a radioactive environment, which will require remote maintenance.

Acknowledgment

This work was supported by Sandia National Laboratories. Some computer calculations were performed at the San Diego Supercomputer Center, which is supported by the National Science Foundation.

Figure Captions

- Fig. 2.1. Overhead view of the light ion fusion LMF target chamber.
- Fig. 3.1. Time integrated target x-ray spectrum from HIBALL type target.
- Fig. 3.2. Peak pressure, vaporized mass and impulse for a 1.5 m radius sphere versus target yield.
- Fig. 3.3. Pressure at graphite wall versus time for 1000 MJ target yield and 1.5 m radius.
- Fig. 4.1. Proposed LMF chamber design.
- Fig. 4.2. Wall perforation patterns.
- Fig. 4.3. Effective elastic constants for a triangular perforation pattern.
- Fig. 4.4. Effective elastic constants for a square perforation pattern.
- Fig. 4.5. Circumferential mechanical stress - the effect of impulsive loading only.
- Fig. 4.6. Circumferential mechanical stress - the effect of impulsive loading and static pressure.
- Fig. 4.7. Fatigue data for 2 1/4 Cr - 1 Mo steel.
- Fig. 4.8. Fatigue data for welded 6061-T6 aluminum.
- Fig. 5.1. Schematic of the chamber models used in the calculations.
- Fig. 5.2. Comparison between pulsed and steady state dose rates at the back of the 2 1/4 Cr -1 Mo steel chamber.
- Fig. 5.3. Comparison between dose rates at the back of the Al 6061-T6 chamber and at a distance of 1 m from the chamber.
- Fig. 5.4. Comparison between contact dose rates behind the chamber.
- Fig. 5.5. Comparison between dose rates at a distance of 1 m from the chamber with borated water.
- Fig. 5.6. Comparison between dose rates at a distance of 1 m from the chamber without borated water.

- Fig. 6.1. X-ray spectrum from a neon gas pinch on PROTO-II. Only the component above 900 eV in photon energy is shown. There is another component to the spectrum below a few hundred eV that has about 4 times the energy but more than 5 times the pulse width.
- Fig. 6.2. Schematic picture of experimental arrangement in PROTO-II.
- Fig. 6.3. Photograph of eight samples shot on SATURN May 1989 with a neon gas puff.
- Fig. 6.4. Photograph of K-Karb after irradiation on SATURN.
- Fig. 6.5. Photograph of aluminum coated with alumina after irradiation on SATURN.
- Fig. 6.6. Photograph of samples after irradiation on SATURN August 1989 with an argon gas puff.